

Old and Young X-ray Point Source Populations in Nearby Galaxies

Edward J. M. Colbert, Timothy M. Heckman, Andy F. Ptak, and David K. Strickland

*Johns Hopkins University, Department of Physics and Astronomy, Homewood Campus,
3400 North Charles Street, Baltimore, MD 21218*

and

Kimberly A. Weaver

*Laboratory for High Energy Astrophysics, Code 662, NASA/GSFC, Greenbelt, MD 20771;
and Johns Hopkins University, Department of Physics and Astronomy, Homewood
Campus, 3400 North Charles Street, Baltimore, MD 21218*

ABSTRACT

We have analyzed Chandra ACIS observations of 32 nearby spiral galaxies and elliptical galaxies and present the results of 1441 X-ray point sources that were detected in these galaxies. The total point-source X-ray (0.3–8.0 keV) luminosity L_{XP} is well correlated with the B-band, K-band, and FIR+UV luminosities of spiral host galaxies, and is well correlated with the B-band and K-band luminosities for elliptical galaxies. This suggests an intimate connection between L_{XP} and both the old and young stellar populations, for which K and FIR+UV luminosities are reasonable proxies for the galaxy mass M and star-formation rate SFR . We derive proportionality constants $\alpha = 1.3 \times 10^{29} \text{ erg s}^{-1} \text{ M}_\odot^{-1}$ and $\beta = 0.7 \times 10^{39} \text{ erg s}^{-1} (\text{M}_\odot \text{ yr}^{-1})^{-1}$, which can be used to estimate the old and young components from M and SFR , respectively. The cumulative X-ray luminosity functions for the point sources have quite different slopes for the spirals ($\gamma \approx 0.6$ –0.8) and ellipticals ($\gamma \approx 1.4$), implying *the most luminous point sources dominate L_{XP}* for the spirals. Most of the point sources have X-ray colors that are consistent with either low-mass X-ray binaries or Ultraluminous X-ray sources (ULXs a.k.a. IXOs) and we rule out classical high-mass X-ray binaries (e.g. neutron-star X-ray pulsars) as contributing much to L_{XP} . Thus, for spirals, the ULXs dominate L_{XP} . We estimate that $\gtrsim 20\%$ of all ULXs found in spirals originate from the older (pop II) stellar populations, indicating that many of the ULXs that have been found in spiral galaxies are in fact pop II ULXs, like those in elliptical galaxies. The *linear* dependence of L_{XP} on the SFR argues for either

a steepening in the X-ray luminosity function of the young (pop I) X-ray source population at $L_X \gtrsim 10^{38.5-39}$ erg s $^{-1}$, or a decreasing efficiency for producing all types of young X-ray point sources as the galaxy SFR increases.

Subject headings: clusters: globular, peanut—bosons: bozos

1. Introduction

As the resolution and sensitivity of X-ray imaging detectors continues to improve, it becomes more and more feasible to study individual X-ray point sources in external galaxies. The point-spread function (PSF) of the Einstein IPC imaging spectrometer ($\sim 1'$) was typically too poor to distinguish emission from individual point sources in galaxies with distances $\gtrsim 2$ Mpc, and, for more nearby galaxies, it was typically only sensitive to very luminous sources with $L_X \gtrsim 10^{38}$ erg s $^{-1}$. The ROSAT PSPC (PSF $\sim 20''$) offered some improvement, and some nearby galaxies could be studied in the soft (0.2–2.4 keV) band. Fabbiano (1989) give a comprehensive review of X-ray sources in nearby galaxies in the pre-Chandra era. The Chandra ACIS instrument has a tremendous improvement in both spatial resolution (PSF $\sim 1''$) and sensitivity, and covers the bandpass 0.2–8.0 keV. We are now able to study the properties of individual point sources in galaxies out to ~ 20 Mpc, for which $L_X \approx 10^{38}$ erg s $^{-1}$ sources are detected in a reasonable (50 ks) exposure time. Although the bright X-ray sources in the Milky Way (MW) are easily studied, many of the MW point sources are viewed through the obscuring galaxy disk and one must attempt to correct for completeness when doing statistical work. Furthermore, in order to study how properties of classes of point sources correlate with host galaxy properties, it is imperative to study large samples of different types of galaxies. We are now able to study properties of low-mass X-ray binaries (LMXBs), high-mass X-ray binaries (HMXBs), Ultraluminous X-ray sources ($L_X \geq 10^{39}$ erg s $^{-1}$; ULXs, a.k.a. Intermediate-luminosity X-ray Objects [IXOs]) in large samples of external galaxies with Chandra.

Hard ($kT \sim 2$ -10 keV) X-ray emission is often present in the halos of elliptical galaxies, and sometimes also in starburst galaxy nuclei (e.g. Moran & Lehnert 1997 and Ptak et al. 1997). ASCA was not able to resolve or diagnose the origin of the hard emission because of its poor spatial resolution (PSF $\sim 1'$). However, Chandra has shown that X-ray *point sources* in spiral and elliptical galaxies often emit a large fraction of the total hard X-ray luminosity. We can now address some important questions with large surveys of galaxies with Chandra. How do the X-ray point source populations of all of the different types of X-ray binaries (XRBs) and ULXs depend on the properties of the host galaxy? What is the exact connection between starbursts (or young star formation) and XRB creation and

evolution? How does the host galaxy environment affect the evolution of the sources? Is there a connection between the XRB population and the ULX population? Here we present results from a study of the properties of the X-ray point source population in a sample of 5 Merger and Irregular galaxies and 18 spiral galaxies, many of which have high young-star formation rates (SFRs), and 9 elliptical galaxies, which typically have negligible SFRs.

In section 2, we describe the galaxy sample. Data reduction techniques are discussed in section 3 and results are given in section 4. We discuss the implications of the results in section 5.

2. Description of Data and Galaxy Sample

The sample was initially selected from nearby ($D < 30$ Mpc) NGC and Messier galaxies that were in the public Chandra archives on September 3, 2001, and were not classical Seyfert galaxies. Proprietary data for galaxies NGC 3079, NGC 3628, NGC 5253 and NGC 4449 were also added. When the Chandra observation of the nearby elliptical galaxy NGC 3379 became public in February 2002, we added it as well. Observations with very low X-ray luminosity sensitivity were omitted by restricting $t/D^2 > 0.044$ ks Mpc $^{-2}$, where t is the exposure time after cleaning (see Table 1), and D is the distance to the galaxy (Table 2). This corresponds to a luminosity sensitivity of $\lesssim 10^{38}$ erg s $^{-1}$ for a back-illuminated (BI) CCD, such as CCD 7. Our goal was to obtain a sizable sample of galaxies of all morphological types, and with a wide range in “starburst power,” since we are interested in studying how the X-ray point source population varies with host galaxy properties.

In Table 2, we list some host galaxy properties that are related the stellar content of the galaxy, in particular properties that are related to the star-formation rate (SFR) and the stellar mass (M). The far-infrared (FIR) and far-ultraviolet luminosities are proxies for the SFR, while the B-band and K_s-band luminosities are proxies for the mass. Note that the galaxies in our sample span a wide range in both morphological type, and in SFR/M (see L_{FIR}/L_B or L_{FIR+UV}/L_K ; Table 2).

For galaxies with recessional velocities < 1000 km s $^{-1}$, as listed in the Third Reference Catalog of Bright Galaxies (RC3; de Vaucouleurs et al. 1991), distances were taken directly from Tully (1988). We used 21-cm recessional velocities when available, otherwise optical recessional velocities. For galaxies with recessional velocities ≥ 1000 km s $^{-1}$, we calculated the distance using $H_0 = 75$ km s $^{-1}$ Mpc $^{-1}$. The distances to NGC 4038 and NGC 5094 were used for X-ray sources in NGC 4038/9 and NGC 5194/5, respectively.

3. Data Reduction

3.1. X-ray Data

All of the ACIS data were retrieved from the SAO Chandra public archives and were reprocessed and reduced using modified versions of the XASSIST v0.757 (Ptak & Griffiths 2003) scripts, LHEASOFT v5.2, and CIAO v2.2.

Level-1 event files were reprocessed to level-2 event files with CIAO, using XASSIST. XASSIST uses the basic data reduction steps recommended by the CXC “threads.” The optional 0.5 pixel position randomization was not performed. After this reprocessing step, each CCD is treated as a different detector, and individual CCD data is processed separately. For data processing, PI values were constrained to be in the range 14–548, corresponding to the energy range 0.2–8.0 keV, although fluxes and counts for X-ray colors were computed from the data in the 0.3–8.0 keV range.

The CIAO WAVDETECT source detection routine was then used on the reprocessed level-2 event data to produce a preliminary list of point sources. For all sources with more than 10 net counts, we further tested the robustness of the detection using a CPU-intensive 2D Gaussian image-fitting algorithm. If a reasonable fit to the image was obtained with a Gaussian (source) plus sloping plane (background) model, we were able to estimate a more accurate count rate, and better estimates of the major and minor axes of the source. If the ratio of the major to minor axis was larger than 2.0, the source was initially flagged as ‘extended.’ Likewise, if the size of the major or minor axes was larger than the PSF (at that off-axis angle), the source was also flagged as ‘extended.’ Sources detected at $S/N < 2.0$ were rejected, as were sources with fitted Gaussian sizes too small to be consistent with the ACIS PSF.

We then filtered only those sources inside the galaxy major and minor R_{25} ellipse, as listed in RC3. Each source was then individually inspected on-screen, and re-classified as ‘point-like’ or ‘extended.’ Any X-ray sources that were within 5” of the galaxy nucleus (as listed in NED) were considered potential active nuclei and were rejected. The ‘jet’ sources in NGC 4258 and Cen A were also rejected. We also rejected all of the artificial X-ray sources that were produced along the readout column of high count-rate sources (NGC 4579 and NGC 5128). After screening, we found a total of 1441 point sources in 32 galaxies (see Table 1).

The major and minor axes for elliptical source regions were determined directly from the Gaussian fitting, or from WAVDETECT if the Gaussian fitting was not performed or failed. Local annular regions surrounding the source, and centered on the source position, were

used for background. In crowded regions, when other source regions overlapped with the background region, the contaminating part(s) of the background region were omitted.

These source and background regions were used directly to compute counts in three energy ranges, for hardness ratios. X-ray fluxes in the 0.3–8.0 keV band were determined for each source using the net count rates from the Gaussian fitting algorithm when available. Otherwise, the count rates from WAVDETECT were used. We converted the count rates to fluxes and luminosities using a simple power-law model with $\Gamma = 1.8$, and the Galactic Hydrogen columns and distances listed in Table 2. Auxiliary Response Files (ARFs) generated using CIAO PSEXTRACT were used to compute fluxes, when they were available. Otherwise, on-axis ARF files were used.

The total galaxy point-source X-ray luminosity L_{XP} was then computed by summing all of the individual X-ray luminosities for each of the point sources (see Table 3). We list in Table 3 the fraction of L_{XP} at $L_X \geq 10^{38}$ erg s $^{-1}$, and the fraction at $L_X \geq 10^{39}$ erg s $^{-1}$ (i.e., the ULXs). We also list the fraction of the total *number* of sources, and the total number of sources in these two high-luminosity ranges. The relatively small scatter in the ratio of L_{XP} to L_K in the last column of Table 3 shows the strong correlation between the stellar light and the X-ray light. As discussed in section 3.2, we believe our values of L_{XP} approximate the actual total point source luminosity within $\sim 20\%$ for most of our galaxies. The exceptions are M82, NGC 253, and the elliptical galaxies, for which we estimate an uncertainty of 40%.

Hardness ratios were computed for all sources with ≥ 20 net counts. A total of 1017 sources met this criterion. Most (810) of these sources were detected on BI CCD 7. One additional source was detected on BI CCD5, and the rest of the sources were detected on front-illuminated (FI) CCDs (0, 1, 2, 3 and 6).

We selected three energy bands for computing hardness ratios: S (soft, 0.3–1.0 keV), M (medium, 1.0–2.0 keV), and H (hard, 2.0–8.0 keV). Counts were extracted directly from the source and background event files described above. Hardness ratios of the form $HR = (C_2 - C_1) / (C_2 + C_1)$ were computed, where C_1 and C_2 are the net counts in the lower and higher energy bands, respectively. Hardness ratios from sources detected on the FI CCDs were transformed to the corresponding ratio for BI CCDs using effective area (EA) curves from the CXC website¹. Corrections to the hardness ratio were obtained by estimating the correction to the counts in each energy band. For each of the sources on the FI CCDs, we first fit a power-law model to spectra in each energy band. We then computed the correction

¹URL http://asc.harvard.edu/cal/Acis/Cal_prods/effarea/4.99/, EA * QE * filt.trans. curve files files orbit_i.dat [FI] and orbit_s.dat [BI]

factor f to the FI counts using the best-fit photon index for that band Γ_{band} and the equation

$$f_{band} = \frac{\int_{band} E^{-\Gamma_{band}} EA(BI) dE}{\int_{band} E^{-\Gamma_{band}} EA(FI) dE}. \quad (1)$$

The corrected counts are then $C1' = f_1 C1$ and $C2' = f_2 C2$, where f_1 and f_2 are the correction factors for the lower and high energy bands, respectively. Corrected hardness ratios HR' were then computed from $HR' = (\phi + HR) / (1 + \phi HR)$, where $\phi = (1 - f_1/f_2)/(1 + f_1/f_2)$.

3.2. Unresolved X-ray Point Sources and Diffuse Hard X-ray Emission

In order to test the accuracy of L_{XP} due to the omission of blended point sources, the erroneous addition of spurious point sources, and “compact” clumps of diffuse emission, we computed the total hard (2.0–8.0 keV) counts from the individual point sources and compared with the total hard counts from the images within the R_{25} ellipse. Hard counts are expected only for point sources (e.g., XRBs) and diffuse hard X-ray emission, since the AGN and jet sources were omitted. In general, the hard counts for each method were consistent within $\sim 20\%$, which is typical of the uncertainty in the total hard counts due to the large number of background counts in the ellipse. For M82 and NGC 253, there were excess hard counts, either in diffuse hard emission, or blended “unresolved” point sources (both are edge-on spiral galaxies). We also found evidence for excess hard counts in the elliptical galaxies. This is expected, since they are well known to have diffuse hard X-ray emission. The diffuse hard emission in elliptical galaxies could be from multiple unresolved XRBs, or could be emission from diffuse, hot gas (e.g., Irwin et al. 2002 and references therein).

3.3. Host Galaxy Luminosities

As mentioned above, we calculated total luminosities from the galaxy in four separate energy bands: FIR, NIR K_s -band, optical B-band, and the far-ultraviolet (FUV). All fluxes were converted to luminosities using the distances listed in Table 2. Far-infrared fluxes over the 40–120 μm band were derived from the 60 μm and 100 μm IRAS fluxes using the method of Fullmer & Lonsdale (1989). Near-infrared K_s -band spectral fluxes F_λ were calculated from 20 mag arcsec^{-2} isophotal magnitudes listed in the 2MASS Large Galaxy Atlas (Jarrett et al. 2003). Optical B-band spectral fluxes F_λ were calculated from B_T^0 magnitudes (or m_B^0 magnitudes for NGC 4038/9) listed in RC3. For NGC 4038/9 and NGC 5194/5, the total spectral flux was calculated using the sum of F_λ for each galaxy. In order to quote all luminosities in roughly the same size band, we have calculated L_K and L_B as λL_λ .

Far-ultraviolet fluxes were estimated using SED-fitting to broad-band total optical magnitudes (usually UBVRI, but in some cases UBVR or UBV), from Prugniel & Heraudeau (1998). We experimented with a wide range of different SED databases, and obtained the best results using the observationally-based SEDS of Kinney & Calzetti (Kinney et al. 1996, Calzetti et al. 1994) and the simulated HYPERZ SEDs (cf. Bolzonella et al. 2000). There was generally good agreement between our estimated FUV fluxes and published measurements (e.g., Rifatto et al. 1995, Marcum et al. 2001). The best-fit SEDs were then integrated from 1500–3500Å to obtain the FUV flux. We list the B, K, FIR and FUV luminosities for each galaxy in Table 2.

4. Results

4.1. Simple Correlations of Total X-ray Point Source Luminosity with Host Galaxy Properties

In Figure 1, we plot the total *point-source* X-ray luminosity L_{XP} against the optical B-band, NIR K-band, FIR and FIR+FUV luminosities of the host galaxy. As noted by Fabbiano et al. (1988), both spiral and elliptical galaxies show a good correlation between the X-ray and B-band luminosity, suggesting that the X-ray luminosity is directly related to the number (or mass) of stars in the galaxy. The NIR K-band luminosity is a more accurate measure of the galaxy stellar mass and we prefer to use it for a proxy for the stellar mass instead of the B-band luminosity.

For all 32 galaxies in our sample, we find that L_K is slightly better correlated with L_{XP} (Pearson correlation coefficient $r=0.93$) than is L_B ($r=0.90$). The best fit yields $L_B \propto L_{XP}^{0.97}$. When elliptical or spiral galaxies are considered separately, for both B and K , the correlation is quite strong, with $r \approx 0.9$ (although $r \approx 0.8$ for B and the spirals).

The FIR luminosity, which is an approximate measure of *current* star formation in late-type spirals and starburst galaxies, is only correlated ($r > 0.50$) with L_{XP} for the Merger/Irr and Spiral galaxies. When all of the galaxies are considered, there is no correlation between L_{FIR} and L_{XP} ($r \approx 0.3$). For ellipticals only, $r \approx 0.1$. We do find that L_{FIR} for the Merger/Irr galaxies, which, in general, have larger SFR/M (Table 2, columns 9 and 10), is better correlated with L_{XP} for the Spiral galaxies ($r=0.93$ vs. 0.68). This suggests that a significant fraction of L_{XP} in high SFR/M galaxies is due to current star formation, whereas in low-to-moderate SFR/mass galaxies, much of L_{XP} could be due to the older population of X-ray sources.

Since some of the light from young, massive stars escapes directly from the galaxy

as UV radiation, we use L_{FIR+UV} ($L_{FIR} + L_{FUV}$) as more accurate proxy for the current SFR. As with L_{FIR} , when all galaxies are considered, there is only a weak correlation ($r \approx 0.5$) between L_{FIR+UV} and L_{XP} . We see a stronger correlation for the Merger/Irr and Spiral galaxies ($r=0.94$ and 0.69 , respectively). For ellipticals only, there is absolutely no correlation ($r \approx 0.01$).

A careful inspection of the $L_{XP} - L_K$ scatter plot in Figure 1 reveals that the Merger/Irr and Spiral galaxies are systematically offset toward larger L_{XP} , when compared to the Elliptical galaxies. This merely illustrates the component of the point-source X-ray luminosity that is due to current star formation and is not directly related to the galaxy stellar mass. We discuss this effect further in section 5.

4.2. X-ray Point Source Luminosity Functions

In Figures 2 and 3, we show the cumulative point source X-ray Luminosity Functions (XLFs) $N(>L)$ for all of the points sources from each of the 32 datasets. We list the slope $\gamma = -d\log N(>L)/d\log L$ for each of the galaxies in Table 4. For the Merger/Irr group, the mean and standard deviation for $\gamma = 0.65 \pm 0.16$, with the most prominent outlier being the dwarf galaxy NGC 5253 with $\gamma \approx 0.9$ (see Table 4). The spirals have very similar slopes: $\gamma = 0.79 \pm 0.24$. The luminosity functions of the elliptical galaxies, however, have steeper slopes, in general: $\gamma = 1.41 \pm 0.38$. The steeper slope for the ellipticals could be indicative of a different mode of X-ray binary formation, or, perhaps more likely, an older LMXB population that is in a later stage of X-ray evolution (e.g., see Grimm et al. 2002 and Wu 2001).

The total point source luminosity L_{XP} can be theoretically defined as

$$L_{XP}^{theor.} = \int_{L_{min}}^{L_{max}} L n(L) dL \propto L_{max}^{1-\gamma} - L_{min}^{1-\gamma}, \quad (2)$$

where, for simplicity, we have assumed $\gamma \neq 1$. Here $n(L)$ is the differential luminosity function [$n(L) = N_0 \gamma L^{-(\gamma+1)}$ when $N(>L) = N_0 L^{-\gamma}$], and L_{min} and L_{max} are the X-ray luminosities of the least and most luminous X-ray point sources in the galaxy, respectively. Since the slope of the cumulative XLF $\gamma < 1$ for the Merger/Irr and spiral galaxies, L_{XP} is most sensitive to the upper limit L_{max} . Although L_{min} and L_{max} are different for each galaxy, in general, the ratio $L_{max}/L_{min} \gtrsim 10^2$ (see Figures 2 and 3), so that the L_{max} term of the integral dominates over the L_{min} term by factors $\gtrsim 5.0$ and $\gtrsim 2.6$, for the Merger/Irr and spiral galaxies, respectively. This is quite interesting, since it implies that for galaxies with shallow XLFs, such as spiral galaxies, the most luminous point sources, such as the

ULXs, dominated L_{XP} . Furthermore, for galaxies with several sources above 10^{38} erg s $^{-1}$, observational measurements of L_{XP} using very deep imaging data sensitive to very faint (e.g., $\gtrsim 10^{36}$ erg s $^{-1}$) sources should give approximately the same value for L_{XP} as a shorter observation sensitive to sources above $\sim 10^{37}$ erg s $^{-1}$. Therefore, we have good reason to believe that the values we quote for L_{XP} in Table 3 are reliable for the spiral galaxies.

4.3. X-ray Color-color diagrams

X-ray color-color (CC) diagrams were constructed using net counts in three X-ray bands, soft (S – 0.3–1.0 keV), medium (M – 1.0–2.0 keV), and hard (H – 2.0–8.0 keV). In our CC diagrams (Figure 4), we plot soft hardness $MS = (M - S)/(M + S)$ against hard hardness $HM = (H - M)/(H + M)$. The Poisson uncertainty in either hardness ratio is nominally $\lesssim 0.3$ (the value for a source with 20 net counts distributed equally in H, M and S). In Figure 5, we show a grid of the expected locations of X-ray sources with a simple power-law spectrum plus foreground absorption. X-ray colors were simulated using the response of BI CCD 7. No foreground absorption corresponds to the lowest values of MS in the diagram, while increasing absorption pushes the source up, and eventually to the right when the medium band (1.0–2.0 keV) begins to be affected by absorption. In Figure 5, we also show the areas of the CC diagrams that would be occupied by LMXBs, NS HMXBs (X-ray pulsars), and (spiral galaxy) ULXs, based on the survey results of Church & Balucinska-Church (2001), Yokogawa (2002), Foschini et al. (2002), and Roberts et al. (2002).

We first examine the CC diagrams of the elliptical galaxies in Figure 4, since they seem to be the least complex. Essentially, all of the point sources from the elliptical galaxies are consistent with LMXBs ($HM \sim -0.5$), with little or no ($N_H < 3 \times 10^{21}$ cm $^{-2}$) absorption. However, note that the range of Γ for ULXs is very similar to that of LMXBs, and, in fact, many of the point sources in the elliptical galaxies have $L_X \geq 10^{39}$ erg s $^{-1}$ (filled circles in Figure 4). Most of the other detected point sources in the elliptical galaxies are also quite luminous, with $L_X > 10^{38.0}$ erg s $^{-1}$. The apparently large fraction of ULXs in ellipticals is due to their luminosity detection limits generally being higher than for nearby spiral bulges, since nearly all of the elliptical are further away than the spirals.

There are a handful of sources that have hard X-ray colors ($HM \sim 0.25$), which is consistent with HMXB X-ray pulsar spectra, but most of the sources have much softer spectra. One would not expect X-ray pulsars in elliptical galaxies. These “hard” sources are exclusively faint, low-luminosity sources, so it is possible that they merely have larger-than-nominal Poisson errors in their X-ray colors.

We next turn to the spiral galaxies (see Figure 4). The point sources are noticeably scattered from the lower left to the upper right, as one might expect for a group of point sources with absorption columns up to $\sim 10^{23} \text{ cm}^{-2}$.

We note that most of the sources in the spiral galaxies are not consistent with NS HMXBs (X-ray pulsars; HM ~ 0.25). They are more consistent with LMXBs or ULXs. As in the ellipticals, only a handful of sources have X-ray colors consistent with NS LMXBs. Most of the ULXs in the spirals seem to have soft ($\Gamma \sim 2$) photon indices. Two ULXs in the Merger/Irr group (which is also the group with the highest values of SFR/M) have harder ($\Gamma < 2$) spectra. X-ray pulsars in the MW and the Magellanic Clouds are typically $\lesssim 10^{37} \text{ erg s}^{-1}$ and contribute very little to the total point-source luminosity, even in the starburst galaxies.

As mentioned previously, the most luminous sources (i.e., the ULXs) dominate L_{XP} in the spiral galaxies and we find here that the X-ray colors of the Chandra ULXs are not consistent with NS HMXBs. Therefore, the total point-source luminosity in spirals is *not* simply dominated by NS HMXBs from the young stellar population, or even by the LMXBs from an older stellar population. It is dominated by soft-spectrum ULXs that curiously seem to have knowledge of (and are correlated with) both the current SFR, as measured by L_{FIR} and L_{FIR+UV} , and the mass of the galaxy, as measured by L_B and L_K . This supports the notion that ULXs are indeed a heterogeneous class of objects (e.g., King 2002). Since the nature of ULXs are not well known, it is premature to say that the X-ray emission from the young stellar population is due to “high-mass X-ray binaries” (e.g. Grimm et al. 2003).

By inspecting the locations of the ULXs in the CC diagrams in Figure 4, one notices that, whereas the ULXs in the elliptical galaxies are clustered near HM ~ -0.4 , the ULXs in the Merg/Irr and Spiral groups are slightly harder in HM. For example, there are no ULXs with HM < -0.4 in the spiral group. This could possibly be a result of obscuration by the gas in spirals, but this would require the ULXs to be highly obscured. As our simulations in Figure 5 (top left plot) show, it takes $N_H \gtrsim 10^{22} \text{ cm}^{-2}$ to move objects $\gtrsim 0.4$ in the +HM direction. Alternatively, this could be a manifestation of two physically different sub-classes of ULXs.

5. Discussion

5.1. Summary of Results

In the previous section, we showed that the total point source X-ray luminosity L_{XP} is indeed correlated with properties of the host galaxy that are associated with the mass

and SFR in the galaxy. Based on the XRB populations in our Galaxy, one might therefore suppose that the correlations merely represent an extrapolation of the total X-ray luminosity from the LMXB and HMXB populations, scaled to the galaxy mass and SFR (e.g., Grimm et al. 2002). However, we argue that the SFR component of L_{XP} is dominated by ULXs, not HMXBs. Since ULXs are not present in our Galaxy, X-ray studies of external galaxies are necessary to understand their effect on X-ray point source populations. Since we can actually measure the correlation between L_{XP} and either L_K or L_{FIR+UV} , both the mass and SFR components of L_{XP} are significantly strong. Since the slope γ of the XLFs is shallow for the spiral galaxies, the most luminous point sources (i.e., the ULXs) dominate L_{XP} . As our CC diagrams show, the X-ray colors of the point sources are generally consistent with LMXBs or ULXs, not HMXBs. This is also true of the most luminous point sources (e.g., the ULXs).

5.2. Multi-variate Correlations Between L_{XP} and Host Galaxy Luminosities

We would like to deconvolve L_{XP} into two components, one from the older stellar population (including LMXBs), and another from the younger stellar population (including HMXBs). We assume the old and young components are directly related to the mass and SFR of the galaxy, respectively, and initially explore a simple relationship between L_{XP} and the host galaxy K and FIR+UV luminosities, which are reasonable proxies for the mass and SFR.

We use the simple linear relationship

$$L_{XP} = AL_K + BL_{FIR+UV}, \quad (3)$$

where A and B are dimensionless constants. We have used χ^2 fitting to estimate A and B and their uncertainties.² The best fit values of A and B are listed in Table 6. Since star formation is negligible in the elliptical galaxies, we can also estimate A directly from L_{XP} by ignoring the SFR term. If we omit the peculiar elliptical galaxy NGC 5128 (Cen A), which has ongoing star-formation, χ^2 -fitting yields $A = 1.26_{-0.31}^{+0.30} \times 10^{-4}$. This value for ellipticals is $\sim 20\%$ larger than that found from multi-variate χ^2 fitting for samples involving Merger/Irr and Spiral galaxies (see Table 6), although the two values are consistent within the uncertainties.

²Errors for L_K and L_{FIR} were estimated from the errors in the flux measurements (see references in notes to Table 2). We estimated a 30% error for the FUV fluxes, due to uncertainties in fitting SEDs to the data (see section 3.3). We also experimented with other fitting methods (principal component analysis, simple least-squares, and robust weighted least-squares) and arrive at the same A and B values, within the χ^2 uncertainties.

Since AGN emission in the K, FIR and FUV bands has not been subtracted from any of the host galaxy luminosities, we computed A and B for two subsamples of galaxies without AGNs, and arrive at a slightly smaller (larger) value for A (B) than if AGNs are included. If the elliptical galaxies are also omitted from the sample, the best fit value of A is also lower. We then suggest that the value of A for early-type and elliptical galaxies is inherently different from that in late-type galaxies.

The fact that A and B are the same order of magnitude, and that L_K and L_{FIR+UV} are also the same order of magnitude, supports our earlier statement that both the old (mass) and young (SFR) component can contribute significantly to L_{XP} .

We conclude, based on our best fit to the Merger/Irr plus spiral sample without AGNs, that the point-source X-ray luminosity L_{XP} in Merger/Irr and spiral galaxies can be reliably estimated from:

$$L_{XP} = (0.9 \pm 0.1 \times 10^{-4})L_K + (0.5 \pm 0.1 \times 10^{-4})L_{FIR+UV}, \quad (4)$$

and that L_{XP} for elliptical galaxies can be estimated from

$$L_{XP} = (1.3 \pm 0.3 \times 10^{-4})L_K. \quad (5)$$

The robustness of this formula for the Merger/Irr and spiral galaxies can be seen in Figure 6 (top), where we plot L_{XP} against the estimated value using equation 4. The Merger/Irr galaxies and Spiral galaxies are both in good agreement, although L_{XP} for the elliptical galaxies is under-estimated. As we argue in the next section, the larger $(M/L)_K$ ratio for ellipticals (see Table 5) likely cause the A value for ellipticals and spirals to be inherently different.

We note that the reduced- χ^2 χ^2_ν for all of the fits (see Table 6) is highly sensitive to the estimated errors in the luminosity uncertainties, which are not well defined. Therefore, we do not use χ^2_ν as an absolute measure of the goodness of fit.

5.3. Multi-variate Correlations between L_{XP} and M and SFR

We next write L_{XP} in terms of the mass M and SFR of the galaxy

$$L_{XP} = \alpha M + \beta SFR, \quad (6)$$

where L_{XP} , M , and SFR have units erg s^{-1} , M_\odot , and $M_\odot \text{ yr}^{-1}$, respectively, and α and β are constants with the appropriate units.

We use the optical/NIR B–K color and the K-band luminosity (Table 2) to estimate the mass of the sample galaxies, and L_{FIR+UV} to estimate the SFR. Bell & de Jong (2001) list correlation coefficients for M/L ratios as a function of optical and NIR colors. We use the coefficients for their formation model with bursts. The SFR can be estimated from L_{FIR+UV} if we assume L_{FIR+UV} is a “corrected” IRAS FIR luminosity. We use a proportionality constant of $5.7 \times 10^{-44} M_{\odot} \text{ yr}^{-1}$ (erg s^{-1}) $^{-1}$, which includes a bolometric correction of 1.4 from the IRAS FIR band (Meurer et al. 1999). The resulting values for SFR, $(M/L)_K$ and M are listed in Table 5.

Again, we find α and β and their uncertainties using minimum- χ^2 techniques. The uncertainties in M and SFR were computed from the uncertainties in all of the luminosities (or magnitudes) used in computing M and SFR. In Table 6, we list the resulting values for the Merger/Irr plus spirals sample (omitting AGNs). We find that the mass-component constant α is slightly different for the elliptical and spiral samples, but this time α is smaller for the ellipticals, although both α values are consistent within their uncertainties. As can be seen in Figure 6 (bottom), after the M/L correction has been made to the mass-component to L_K , L_{XP} estimated using α and β for the spirals agrees well with the observed L_{XP} , even for the elliptical galaxies. This indicates that $\alpha = 1.25 \times 10^{29} \text{ erg s}^{-1} M_{\odot}^{-1}$ is a *universal constant* for estimating the point-source X-ray luminosity from the older stellar population.

Thus, we find the following empirical relationship to hold for high-SFR/M Merger/Irr galaxies, spiral galaxies, and low-SFR/M elliptical galaxies:

$$L_{XP}(\text{erg s}^{-1}) = (1.3 \pm 0.2 \times 10^{29})M(M_{\odot}) + (0.7 \pm 0.2 \times 10^{39})SFR(M_{\odot} \text{ yr}^{-1}) \quad (7).$$

As noted in the caption to Figure 6, the observed values for L_{XP} for the two starburst galaxies NGC 4449 and NGC 4038/9 are in excess of the values predicted by Equations (4) and (7), by factors of ≈ 4 and ≈ 5 , respectively. Since L_{XP} is dominated by the *SFR* component for starburst galaxies, an error in the *SFR* by ~ 4 – 5 would be needed to “correct” the problem. This is unlikely. Poisson uncertainty in the number of high-luminosity sources (which dominate L_{XP}) could possibly explain the excess, but it is also possible that these two starburst galaxies have significantly high efficiency for forming luminous BH XRBs and ULXs. It is interesting that NGC 4038/9 is a merging system and NGC 4449 has evidence for two physical counter-rotating systems within the galaxy (Sabbadin et al. 1984). More extensive tests would be needed to determine if merger activity is really responsible for the abnormally high values of L_{XP} in these two galaxies.

5.4. Nature of the X-ray Point Sources

As mentioned previously, we assume the mass component of L_{XP} is from point sources from an older stellar population (including LMXBs), and the SFR component is from point sources from a younger stellar population (including HMXBs). It is not known if ULXs, which can dominate L_{XP} (section 4.2), are predominantly associated with older or younger stellar population, or are a largely heterogeneous group. Thus, they could contribute significantly in either component. We know that ULXs in elliptical galaxies (e.g. Colbert & Ptak 2002) are from older populations, since they have negligible star formation. On the other hand, in the high-SFR galaxy pair NGC 4038/9 (The “Antennae”), L_{FIR} is very high and an extraordinarily large number of ULXs are found (Fabbiano, Zezas & Murray 2001), suggesting that the ULXs in the Antennae are associated with the young stellar population. So what about ULXs in the normal spirals, in which old and young stellar populations (ie the K and FIR+UV luminosities) can be comparable?

In Figure 7, we plot the fraction of L_{XP} from the younger stellar population against galaxy morphological type. As expected, in late-type galaxies with high SFR/M ratios, the SFR term dominates, and in early-type galaxies, the mass term dominates. This plot also shows that the older population contributes $\approx 20\text{--}90\%$ of L_{XP} in Merger/Irr and spiral galaxies. As described in section 4.2, since the slope of the XLF for these groups is shallow ($\gamma \lesssim 1$), the most luminous X-ray point sources dominate L_{XP} . This would imply that, if the old and young components of the XLF have exactly the same shape, $\sim 20\text{--}90$ percent of the ULXs are from the older population. However, this is not likely to be the case since the XLFs for older point sources in the elliptical galaxies is much steeper than the XLFs for old+young point sources in the spirals, and many of the ULXs are from the younger population. However, it does suggest that type II (pop II) ULXs could have significant numbers in spiral galaxies. Since we now know that L_{XP} from the older stellar population is proportional to the galaxy mass M , we can estimate the fraction of type II ULXs in spirals by scaling the number found in ellipticals by the galaxy mass M . If we exclude NGC 5128 since it has ongoing star formation, the total mass of the remaining eight ellipticals is $1.06 \times 10^{12} M_{\odot}$, and eleven ULXs are found. This implies an expected 1.0×10^{-11} ULXs M_{\odot}^{-1} , with a Poisson error of 30%. The total mass of all of the Merg/Irr and spiral galaxies is $6.6 \times 10^{11} M_{\odot}$, so we expect $\approx 5\text{--}9$ pop II ULXs to be found. A total of 32 ULXs were detected, implying that, on average, $\sim 15\text{--}25\%$ of the ULXs in Merger/Irr and spiral galaxies are pop II ULXs. The same calculation for the Merger/Irr and spiral galaxy samples alone yield rates of $\sim 5\text{--}10\%$ and $\sim 25\text{--}50\%$ of pop II ULXs for the “high-SFR/M” Merger/Irr galaxies, and normal spirals, respectively.

5.5. Theoretical Considerations

Although the point-source luminosity L_{XP} is a quantity that can easily be measured, it is perhaps more intuitive to assume that the normalization n_0 of the differential luminosity function [where $n(L) = n_0 L^{-(\gamma+1)}$] is the quantity that is proportional to M and SFR . The quantity $n(L)$ is a measure of the number of point sources as a function of the type of object (ordered by luminosity), so if the mass or SFR increases, one would assume that the old and young components of $n(L)$ would increase proportionally, so that

$$n(L) = \mu M L^{-\alpha_M} + \nu SFR L^{-\alpha_{SFR}}, \quad (8)$$

where μ and ν are constants, and α , the slope of $n(L)$, is related to the slope γ of the cumulative luminosity function $N(>L)$ by $\alpha = \gamma + 1$.

As described in section 4.2, γ for the elliptical galaxies ≈ 1.4 , so $\alpha_M \approx 0.4$. The value of α_{SFR} can be estimated from γ for galaxies with very high SFR/M ratios. We can write L_{XP} as

$$L_{XP} = \int_{L_{min}}^{L_{max}} n(L) L dL = \mu M \int_{L_{min}}^{L_{max}^M} L^{1-\alpha_M} dL + \nu SFR \int_{L_{min}}^{L_{max}^{SFR}} L^{1-\alpha_{SFR}} dL, \quad (9)$$

where the lower limit L_{min} is the sensitivity limit of the observation, and the upper limit L_{max} is the luminosity of the most luminous (old or young) point source, respectively. Equation 9 looks very similar to our observational result $L_{XP} = \alpha M + \beta SFR$. However, the upper limit L_{max} depends on M (or SFR). To see this, note that L_{max} can be estimated from the luminosity for which the cumulative luminosity function $N(>L) = N_0 L^{-\gamma} \approx 1$, i.e. $L_{max} \approx N_0^{1/\gamma}$, so that $L_{max}^M \propto M^{1/\gamma_M}$ and $L_{max}^{SFR} \propto SFR^{1/\gamma_{SFR}}$. If we now use these estimates for L_{max} and integrate Eqn. (9), we find

$$L_{XP} = \left(\frac{\mu}{1 - \gamma_M} \right) M \left(C_M^{1-\gamma_M} M^{\frac{1}{\gamma_M} - 1} - L_{min}^{1-\gamma_M} \right) + \left(\frac{\nu}{1 - \gamma_{SFR}} \right) SFR \left(C_{SFR}^{1-\gamma_{SFR}} SFR^{\frac{1}{\gamma_{SFR}} - 1} - L_{min}^{1-\gamma_{SFR}} \right), \quad (10)$$

where C_M and C_{SFR} are constants relating M and SFR to L_{max} (e.g. $L_{max}^M = C_M M^{1/\gamma_M}$). For simplicity, we have assumed here that $\gamma_M \neq 1$ and $\gamma_{SFR} \neq 1$. Since $\gamma_M \approx 1.4$, $\frac{1}{\gamma_M} - 1 \approx -0.3$, so there is only a weak dependence on M for the L_{max} term of the mass integral. As discussed in section 4.2, the L_{min} term of the mass integral dominates for $\gamma > 1$, so the weak mass dependence of the L_{max} term will be washed out by the mass-independent L_{min} term, and L_{XP} should be very nearly linear in M . In fact, this is what we find experimentally. A least-squares fit between $\log L_{XP}$ and $\log M$ for the eight elliptical galaxies in our sample with

no star formation (NGC 5128 omitted) implies a best fit for $L_{XP} \propto M^{0.99}$ ($r = 0.89$). A more rigorous test from a multi-variate fit to the sample of 18 Merg/Irr and spiral galaxies without AGN gives the best fit for mass component of $L_{XP} \propto M^{1.01}$ (See Figure 8). Therefore, we can argue with good confidence that the old component of L_{XP} is essentially linear in M .

The situation for the SFR component of L_{XP} is more complex. As mentioned in section 4.2, the L_{min} term of Equation 10 is negligible for such a shallow slope of $\gamma \sim \gamma_{Merg/Irr} \approx 0.65$, which implies that the SFR component of $L_{XP} \propto SFR^{1/\gamma_{SFR}}$. Although it is not possible to measure γ_{SFR} directly in a typical normal spiral galaxies, we can assume that the mass component of the XLF in the high SFR/M galaxies is much fainter than the SFR component, so that $\gamma_{SFR} \sim \gamma_{Merg/Irr} \approx 0.65$ is a reasonable assumption. We would then expect the SFR component of $L_{XP} \propto SFR^{1.5}$. However, this is not what we find. A multi-variate fit to $L_{XP} = \alpha M + \beta SFR^{p_{SFR}}$ give a best fit for $p_{SFR} = 1.06$, with a 90% confidence range of 0.85–1.25 (for three free parameters: $\Delta\chi^2 < 6.25$; see Figure 8). As a check, if we fit $\log L_{XP}$ to $\log SFR$ for the 5 high SFR/M Merger/Irr galaxies, it also implies a much smaller exponent: $L_{XP} \propto SFR^{1.09}$ ($r = 0.94$).

It is interesting to note that the best-fit exponent is slightly larger than unity, as our simple model predicts it should be. The implied value of $\gamma_{SFR} = 1/p_{SFR} \approx 0.90\text{--}0.95$. This suggests that our assumption that $N(>L)$ is a simple power-law is incorrect.

One explanation is that the slope steepens at high luminosity. If, for example, BH HMXBs and type I ULXs form in a much different manner than “normal” HMXBs, one might expect a break in the XLF at the luminosity that separates the two classes of point sources. Thus, our result could be interpreted as suggestive evidence for a break in the luminosity function at high (“near-ULX”) luminosities. This scenario might also be explained as an aging effect, since, to first order, the highest luminosity sources spend their fuel at a faster rate and therefore have shorter X-ray lifetimes (e.g. Wu 2001).

Unfortunately, it is quite difficult to measure the slope of the XLF at high luminosities in most galaxies. The Poisson uncertainty in the number of sources at the high end of the XLF is quite large compared to the actual number of sources, and careful statistical fitting techniques must be used. The Antennae galaxies have a large number of high-luminosity sources (~ 14 ULXs; Table 3) and are perhaps the best laboratory for testing for a break in the XLF. By inspection of the XLF of NGC 4038/9 shown in Figure 2, there *appears* to be a break at $\log L_{XP} \approx 39.5$. However, in a careful analysis of the Antennae’s XLF, Zezas & Fabbiano (2002) claim that a simple power-law is statistically consistent with the data. It would be useful to use XLFs of massive and powerful starbursting systems like the Antennae, or perhaps a combined XLF from a large number of starburst galaxies, to do a careful test to determine if there is indeed evidence for a break at luminosities $\sim 10^{38.5\text{--}39}$ erg s^{−1}, where

there are normally very few sources per galaxy.

Another possible explanation is that the normalization n_0 of the pop I differential luminosity function is *not* linear in the SFR, as we assumed. In other words, it is not merely the high-luminosity X-ray sources that are reduced, but rather most, or all, of the X-ray sources. In order to yield our best-fit exponent $p_{SFR} = 1.06$, this would imply (see Equation 10) that $n_0 \propto \text{SFR}^{-0.5}$ for $\gamma_{SFR} = 0.65$. This scenario would imply that the formation efficiency of X-ray point sources somehow becomes less and less efficient with increasing SFR. Future XLF work will all important tests for discriminating between these two scenarios.

We are grateful to T. Jarrett for providing 2MASS K_s magnitudes from the Large Galaxy Atlas before publication. We thank A. Zezas, T. Roberts, T. Yaqoob and A. Prestwich for helpful discussions, and T. Budavari for expert help with SED fitting.

REFERENCES

Bell, E. F., & de Jong, R. S. 2001, ApJ, 550, 212

Bolzonella, M., Miralles, J.-M., & Pello, R. 2000, A&A, 363, 476

Calzetti, D., Kinney, A. L., & Storchi-Bergmann, T. 1994, ApJ, 429, 582

Church, M. J., & Balucinska-Church, M. 2001, A&A, 369, 915

Colbert, E. J. M., & Ptak, A. F. 2002, ApJS, 143, 25

Dickey, J. M., & Lockman, F. J. 1990, ARA&A, 28, 215

de Vaucouleurs, G., de Vaucouleurs, A., Corwin, H. G., Buta, R. J., Paturel, G., & Fouque, P. 1991, Third Reference Catalog of Bright Galaxies (RC3; New York: Springer-Verlag)

Fabbiano, G. 1989, ARA&A, 27, 87

Fabbiano, G., Gioia, I. M., & Trinchieri, G. 1988, ApJ, 324, 749

Fabbiano, G., Zezas, A., & Murray, S. S. 2001, ApJ, 554, 1035

Foschini, L., et al. 2002, A&A, 392, 817

Fullmer, L., & Lonsdale, C. 1989, Cataloged Galaxies and Quasars in the IRAS Survey (JPL Pub. D-1932, Version 2, Appendix B)

Grimm, H.-J., Gilfanov, M., & Sunyaev, R. 2002, A&A, 391, 923

Grimm, H.-J., Gilfanov, M., & Sunyaev, R. 2003, MNRAS, 339, 793

Ho, L. C., Filippenko, A. V., & Sargent, W. L. W. 1997, ApJS, 112, 315

Irwin, J. A., Sarazin, C. L., & Bregman, J. L. 2002, ApJ, 570, 152

Jarrett, T. H., Chester, T., Cutri, R., Schneider, S., & Huchra, J., 2003, AJ, 125, 525

King, A. R. 2002, MNRAS, 335, L13

King, A. R., Davies, M. B., Ward, M. J., Fabbiano, G., & Elvis, M. 2001, ApJ, 552, L109

Kinney, A. L., Calzetti, D., Bohlin, R. C., McQuade, K., Storchi-Bergmann, T., & Schmitt, H. R. 1996, ApJ, 467, 38

Knapp, J. 1994, priv. comm. to NED (correction to data from Knapp et al. 1989)

Knapp, G. R., Guhathakurta, P., Kim, D.-W., & Jura, M. A. 1989, ApJS, 70, 329

Marcum, P. M., et al. 2001, ApJS, 132, 129

Meurer, G. R., Heckman, T. M., & Calzetti, D. 1999, ApJ, 521, 64

Moshir, M., et al. 1992, Explanatory Supplement to the IRAS Faint Source Catalog, version 2, JPL D-10015 (Pasadena: JPL)

Moran, E. C., & Lehnert, M. D. 1997, ApJ, 478, 172

Prugniel, Ph., & Héraudeau, Ph. 1998, A&AS, 128, 299

Ptak, A., & Griffiths, R. 2003, in Astronomical Data Analysis Software & Systems XII, eds. H. Payne, R. Jedrzejewski, & R. Hook, ASP conference series vol. 295, 465

Ptak, A., Serlemitsos, P., Yaqoob, T., Mushotzky, R., & Tsuru, T. 1997, AJ, 113, 1286

Rice, W., et al. 1988, ApJS, 68, 91

Rifatto, A., Longo, G., & Capaccioli, M. 1995, A&AS, 114, 527

Roberts, T. P., Goad, M. R., Ward, M. J., Warwick, R. S., & Lira, P. 2002, in “New Visions of the X-ray Universe in the XMM-Newton and Chandra Era,” (ESTEC: The Netherlands) (astro-ph/0202017)

Sabbadin, F., Ortolani, S., & Bianchini, A., 1984, A&A, 131, 1

Sandage, A., & Tammann, G. A. 1981, Revised Shapley-Ames Catalog of Bright Galaxies (Carnegie Institute of Washington Publication 635)

Soifer, B. T., Boehmer, L., Neugebauer, G., & Sanders, D. B. 1989, AJ, 98, 766

Thronson, H. A., Jr., Hunter, D. A., Telesco, C. M., Decher, R., & Harper, D. A. 1987, ApJ, 317, 180

Tully, R. B. 1988, Nearby Galaxies Catalog (Cambridge: Cambridge Univ. Press)

Wu, K. 2001, PASA, 18, 443

Yokogawa, J., 2002, Ph. D. Thesis, Kyoto University

Zezas, A., & Fabbiano, G. 2002, ApJ, 577, 726

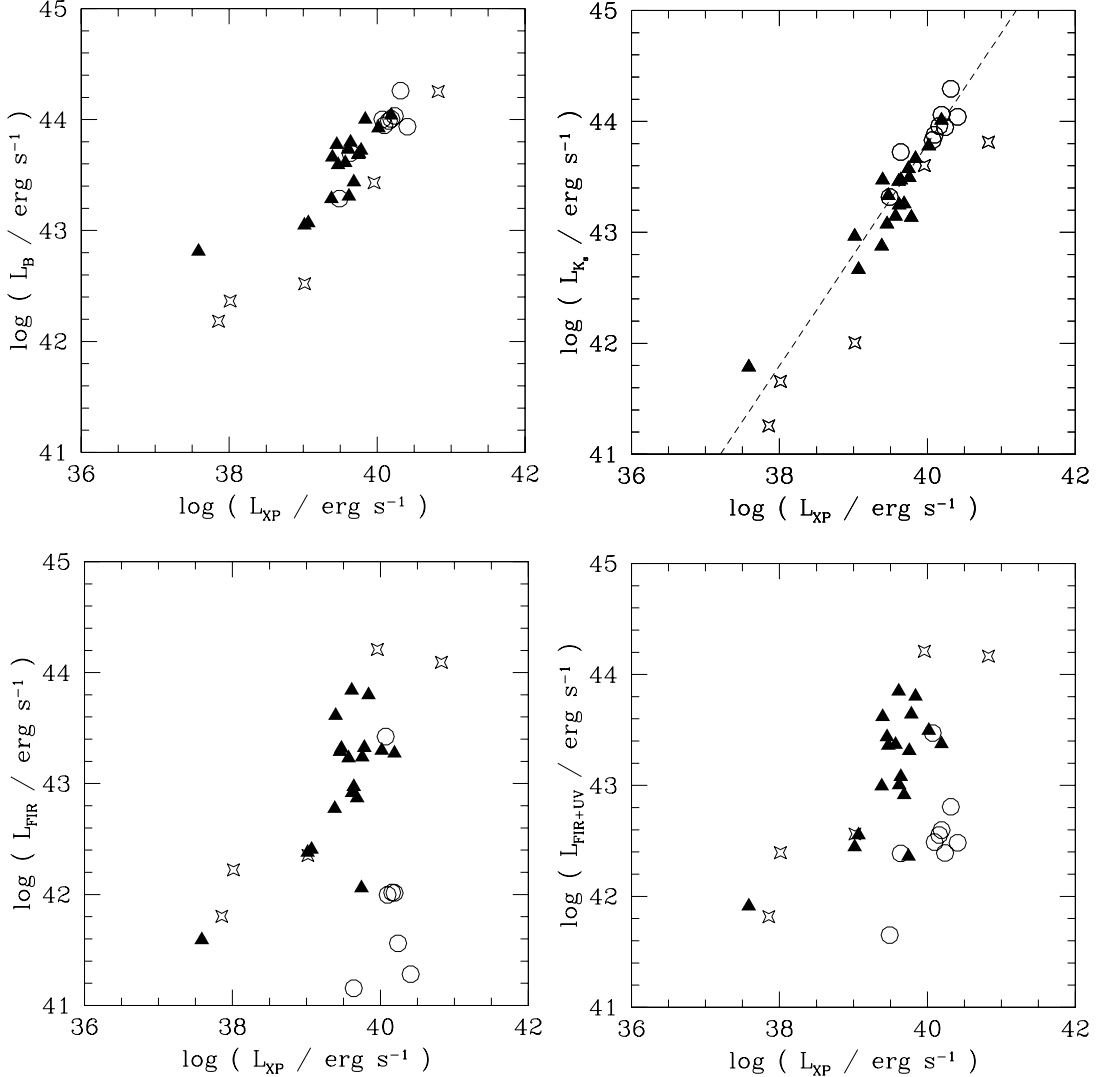


Fig. 1.— Correlations of X-ray Point Source Luminosity L_{XP} with Host Galaxy Properties. **Upper left:** L_B vs. L_{XP} ; **Upper right:** L_{K_s} vs. L_{XP} . The dashed line indicates the best fit linear correlation for only the Elliptical galaxies (see text section 4.1); **Lower left:** L_{FIR} vs. L_{XP} ; **Lower right:** L_{FIR+UV} vs. L_{XP} ; Four-pointed starred symbols represent Merger/Irregular galaxies, filled triangles are Spiral galaxies, and open circles are Elliptical galaxies (see section 2 and Table 1).

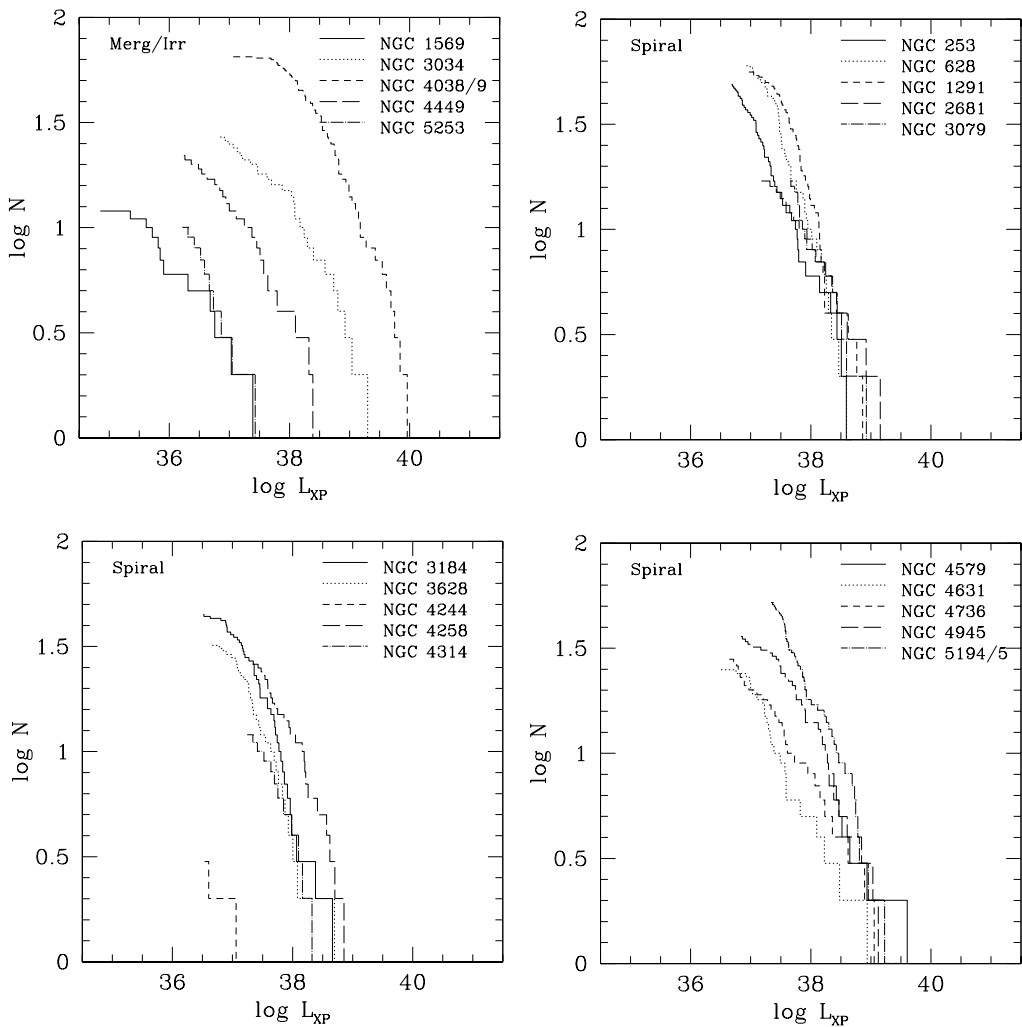


Fig. 2.— Cumulative X-ray Point Source Luminosity Functions for Merger/Irregular and Spiral galaxies. See section 4.2 for details.

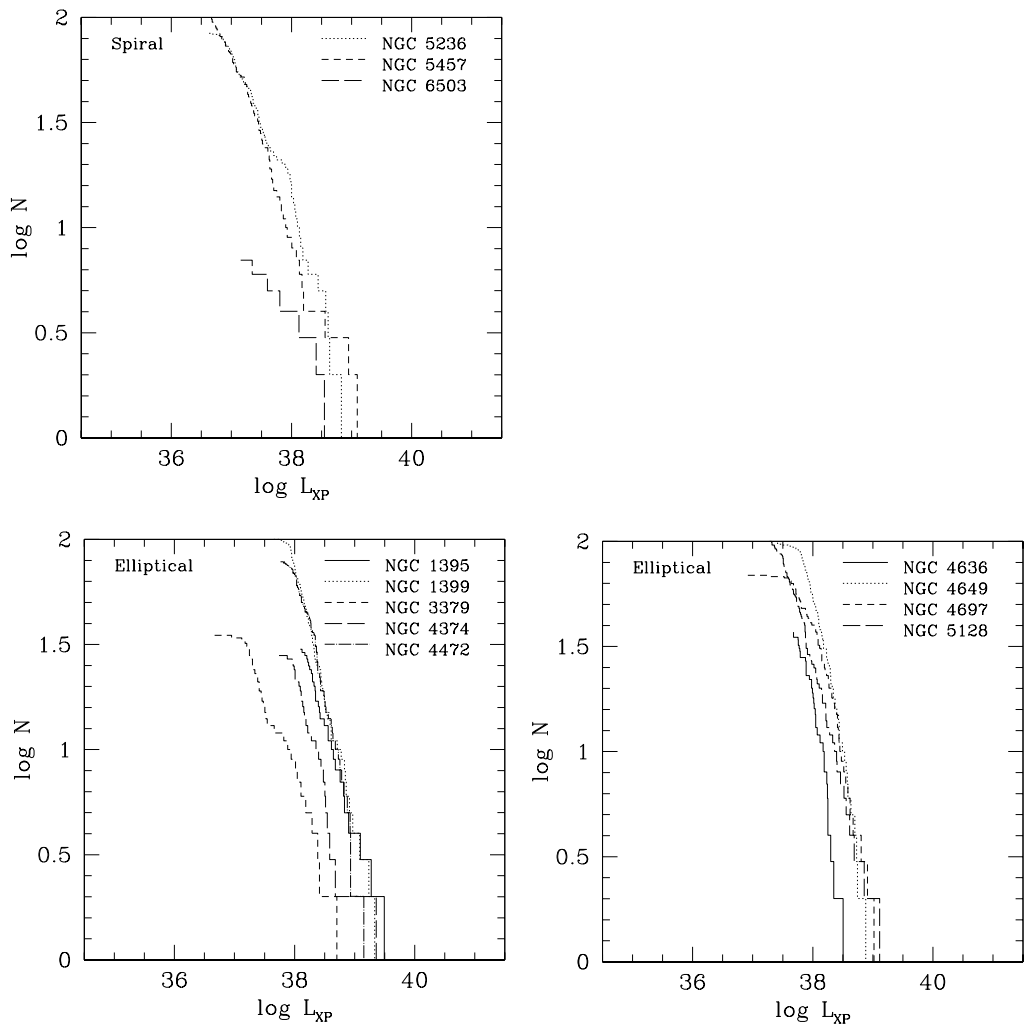


Fig. 3.— Cumulative X-ray Point Source Luminosity Functions for Spiral and Elliptical galaxies. See section 4.2 for details.

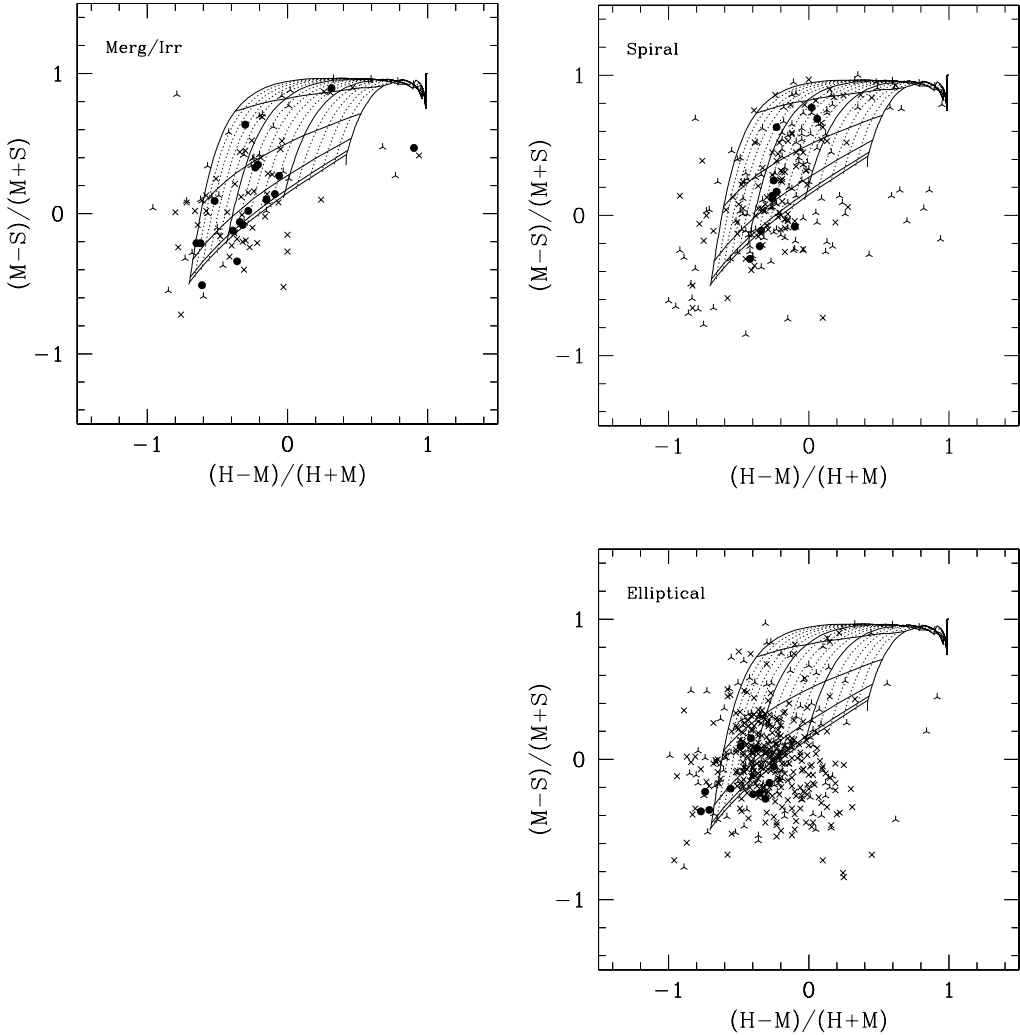


Fig. 4.— X-ray color-color diagrams for galaxy grouped by morphological type, as listed in Table 1 (see section 2). See sections 3.1 and 4.3 for discussion of the hardness ratio calculations. **(upper left)** Merger and Irregular galaxies; **(upper right)** Spiral galaxies; and **(lower right)** Elliptical galaxies. Objects marked by skeletal triangular symbols have $L_X < 10^{38} \text{ erg s}^{-1}$, while those marked by an 'X' have $10^{38} \geq L_X < 10^{39} \text{ erg s}^{-1}$. ULXs i.e., those with $L_X \geq 10^{39} \text{ erg s}^{-1}$, are marked by filled circles. The grid shows how absorption effects push sources up and to the right in the diagram (see Figure 5 for details).

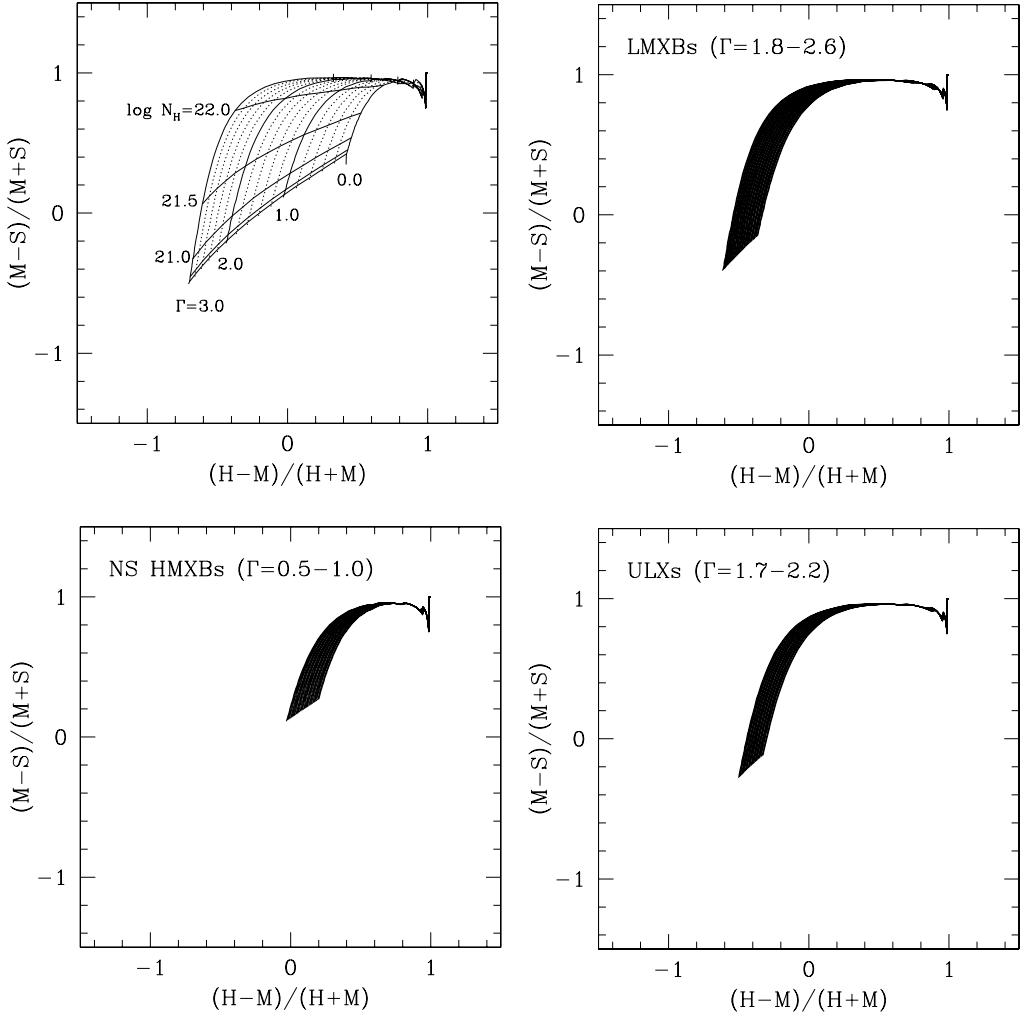


Fig. 5.— Spectral Properties of Sources in X-ray color-color diagrams. **(upper left)** X-ray colors of sources with power-law spectra with photon index Γ ranging from 0.0 to 3.0 in steps of 0.2, and neutral Hydrogen column N_H ranging from 0.0 to $100.0 \times 10^{22} \text{ cm}^{-2}$. In the upper left plot, the five contours for N_H are for $N_H = 0.01, 0.03, 0.1, 0.3$ and $1.0 \times 10^{22} \text{ cm}^{-2}$. The four tick marks at $(M - S)/(M + S) \approx 1.0$ correspond to $N_H = 3.0 \times 10^{22} \text{ cm}^{-2}$. **(upper right)** Area of the color-color diagram occupied by Milky Way LMXBs, which typically have $\Gamma \sim 1.8 - 2.6$ (e.g., Church & Balucinska-Church 2001). **(lower left)** Area occupied by NS HMXBs (X-ray pulsars, $\Gamma \sim 0.5 - 1.0$; e.g., Yokogawa 2002). **(lower right)** Area typically occupied by ULXs ($\Gamma \sim 1.7 - 2.2$; e.g., Foschini et al. 2002 and Roberts et al. 2002).

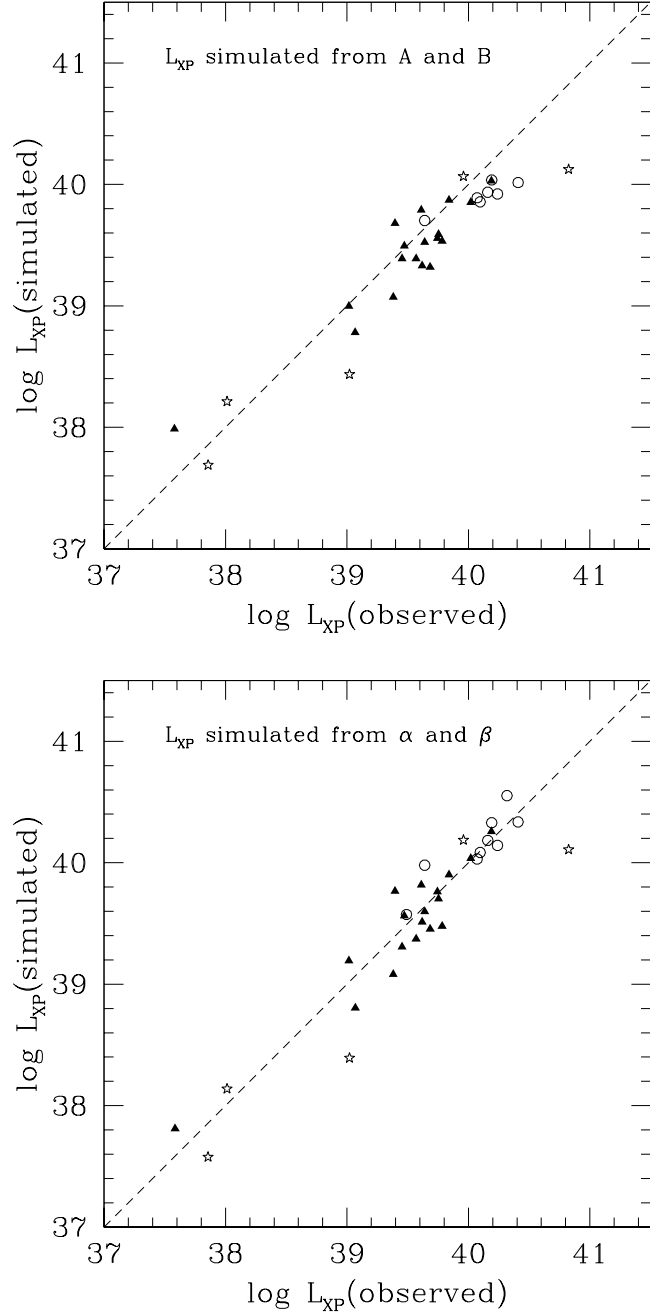


Fig. 6.— **(top)** Simulated X-ray point source luminosity L_{XP} , calculated from A , B , L_K , and L_{FIR+UV} . **(bottom)** Simulated X-ray point source luminosity L_{XP} , calculated from α , β , M , and SFR . The dashed line indicates $L_{XP}(\text{simulated}) = L_{XP}(\text{observed})$. Merger/Irregular galaxies are shown as starred symbols, spiral galaxies as filled triangles, and elliptical galaxies as open circles. Axes are in units of $\log \text{erg s}^{-1}$. The values used for A , B , α , and β are those tabulated for the “only M/I and spiral galaxies, no AGN” sample in Table 6. Note that the elliptical galaxies deviate in the upper plot, while two starburst galaxies (NGC 4449 at $\log L_{XP}(\text{observed}) = 39.0$, and NGC 4038/8 at $\log L_{XP}(\text{observed}) = 40.8$) deviate in both plots.

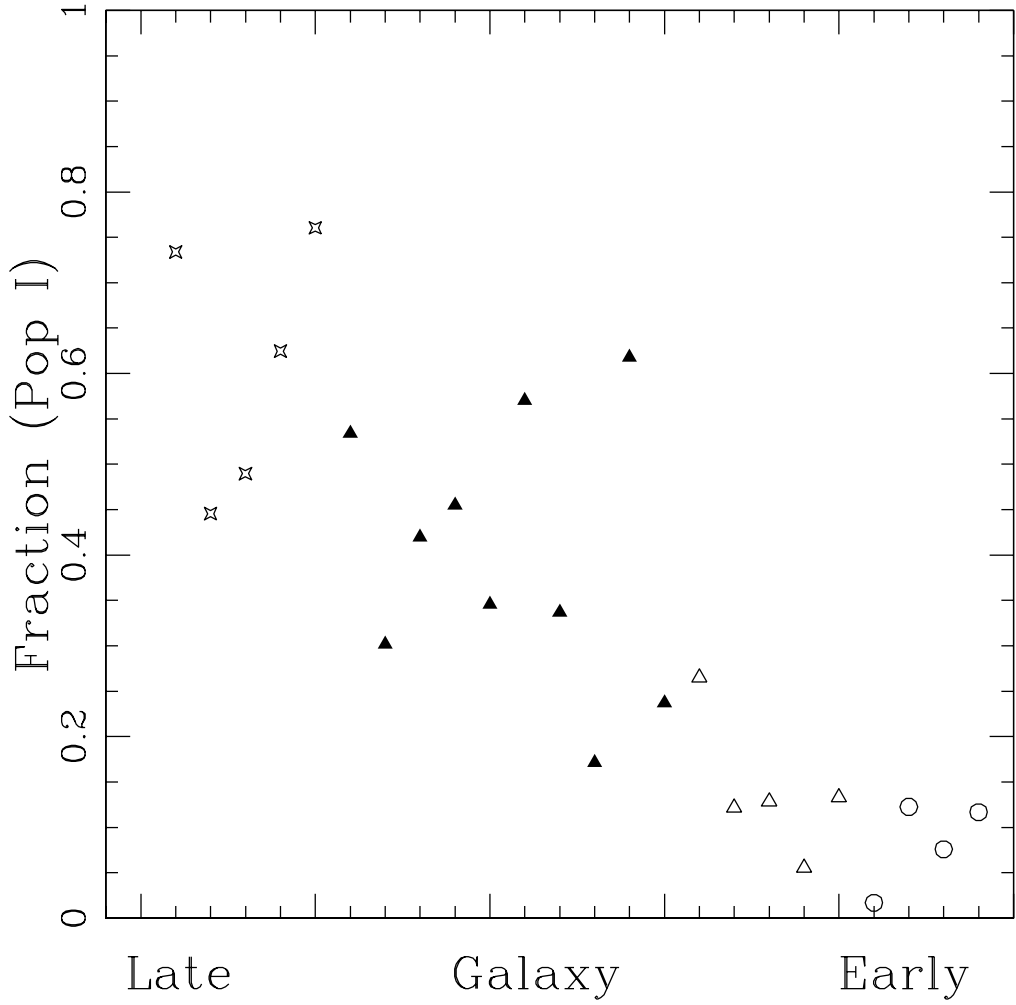


Fig. 7.— Fraction of simulated L_{XP} from the young X-ray point source population (pop I): Fraction (Pop I) = $\beta SFR / (\alpha M + \beta SFR)$. All elliptical galaxies have been omitted except for NGC 5128, since we have no reliable estimate for their SFR. The abscissa indexes the galaxies in order of morphological type, from late to early, based on the types listed in Table 2. Merger/Irregular galaxies are plotted as starred symbols, Scd/Sc spirals are plotted as filled triangles, Sbc/Sb/Sab spirals plotted as open triangles, and Sa/S0 galaxies plotted as open circles.

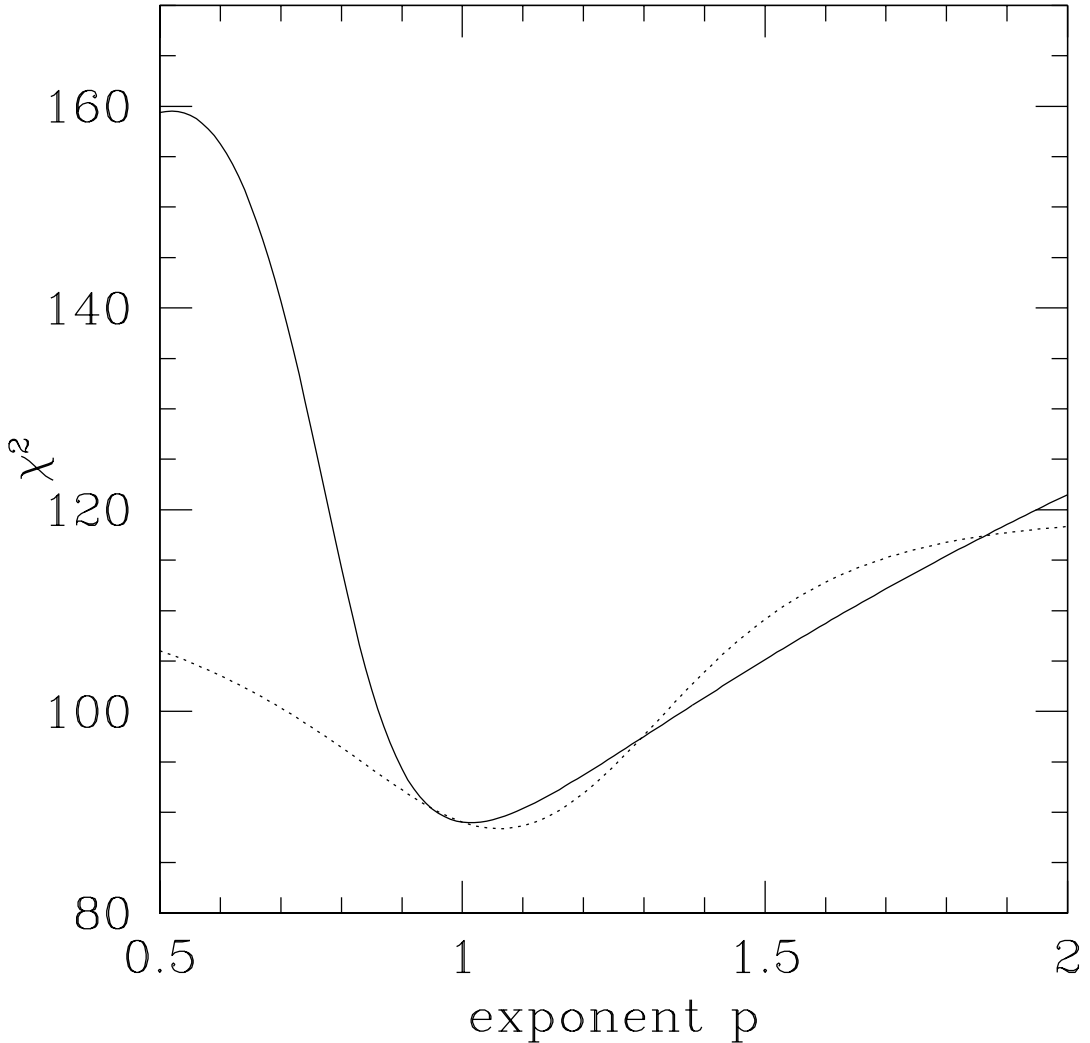


Fig. 8.— Chi-square values for multivariate fits for non-linear dependence of L_{XP} on M and SFR . The solid line shows χ^2 for a linear SFR term and a simple power-law for the M term: $L_{XP}(\text{pop I}) \propto SFR$ and $L_{XP}(\text{pop II}) \propto M^{p_M}$. The dotted line shows χ^2 for the opposite dependence: a linear M term and a power-law SFR term: $L_{XP}(\text{pop I}) \propto SFR^{p_{SFR}}$ and $L_{XP}(\text{pop II}) \propto M$. The best-fit minimum- χ^2 power-law exponents are $p_M = 1.01_{-0.11}^{+0.23}$ and $p_{SFR} = 1.06_{-0.21}^{+0.19}$, where the errors are 90% confidence for 3 free parameters ($\Delta\chi^2 \leq 6.25$).

Table 1. Observational Data

| Galaxy Name (1) | Other Name (2) | ObsID (3) | CCDs (4) | Exp. Time (ks) (5) | N (6) |
|--------------------|-------------------|--------------|-------------|--------------------------|----------|
| NGC 1569 | | 782 | 7 | 85.1 | 12 |
| NGC 3034 | M82 | 361 | 0/1/2/3 | 33.2/32.8/33.1/33.0 | 27 |
| NGC 4038/9 | Antennae | 315 | 6/7 | 72.1/70.2 | 65 |
| NGC 4449 | | 2031 | 7 | 26.2 | 22 |
| NGC 5253 | | 2032 | 7 | 46.7 | 10 |
| NGC 253 | | 969 | 2/3/6/7 | 13.9/13.9/13.9/11.8 | 49 |
| NGC 628 | M74 | 2057 | 6/7 | 46.2/44.7 | 60 |
| NGC 1291 | | 2059 | 6/7 | 11.2/12.0 | 56 |
| NGC 2681 | | 2061 | 7 | 78.3 | 17 |
| NGC 3079 | | 2038 | 7 | 26.3 | 17 |
| NGC 3184 | | 804 | 7 | 37.1 | 45 |
| NGC 3628 | | 2039 | 7 | 54.8 | 32 |
| NGC 4244 | | 942 | 7 | 48.1 | 3 |
| NGC 4258 | M106 | 350 | 6/7 | 14.0/13.9 | 26 |
| NGC 4314 | | 2062 | 7 | 8.3 | 12 |
| NGC 4579 | M58 | 807 | 7 | 32.8 | 8 |
| NGC 4631 | | 797 | 6/7 | 59.1/57.6 | 25 |
| NGC 4736 | M94 | 808 | 7 | 47.3 | 28 |
| NGC 4945 | | 864 | 6/7 | 35.2/5.1 | 36 |
| NGC 5194/5 | M51a/b | 354 | 6/7 | 14.8 | 52 |
| NGC 5236 | M83 | 793 | 6/7 | 50.9/48.2 | 84 |
| NGC 5457 | M101 | 934 | 2/3/5/6/7 | 98.1/98.1/96.3/98.2/95.6 | 140 |
| NGC 6503 | | 872 | 7 | 9.1 | 7 |
| NGC 1395 | | 799 | 3 | 22.2 | 30 |
| NGC 1399 | | 319 | 7 | 55.5 | 100 |
| NGC 3379 | M105 | 1587 | 7 | 31.0 | 35 |
| NGC 4374 | M84 | 803 | 7 | 28.3 | 28 |
| NGC 4472 | M49 | 321 | 6/7 | 39.2/33.8 | 78 |
| NGC 4636 | | 323 | 7 | 45.2 | 37 |
| NGC 4649 | M60 | 785 | 6/7 | 36.7/22.3 | 98 |
| NGC 4697 | | 784 | 7 | 39.0 | 69 |
| NGC 5128 | Cen A | 316 | 0/1/2/3 | 35.5/35.3/35.4/35.5 | 133 |

Notes on table columns: (1,2) Galaxy Names; (3) Chandra Observation ID; (4) ACIS CCD numbers in galaxy FOV for which point sources were detected; (5) Exposure time for CCDs listed in column 4; (6) Number of X-ray point sources detected within galaxy FOV (see section 3 for details).

Table 2. Galaxy Properties

| Galaxy Name (1) | Distance (Mpc) (2) | Morph. Type (3) | AGN Type (4) | L_B (\log erg/s) (5) | L_K (\log erg/s) (6) | L_{FIR} (\log erg/s) (7) | L_{UV} (\log erg/s) (8) | $\frac{L_{FIR}}{L_B}$ (9) | $\frac{L_{FIR+UV}}{L_K}$ (10) |
|-----------------|--------------------|-----------------|--------------|---------------------------|---------------------------|-------------------------------|------------------------------|---------------------------|-------------------------------|
| NGC 1569 | 1.6 | Sm | | 42.2 | 41.3 | 41.8 | 40.3 | 0.4 | 3.6 |
| NGC 3034 | 5.2 | I0 | | 43.4 | 43.6 | 44.2 | 41.7 | 6.0 | 4.0 |
| NGC 4038/9 | 21.7 | Sc/Sc (tides) | | 44.3 | 43.8 | 44.1 | 43.4 | 0.7 | 2.2 |
| NGC 4449 | 3.0 | Sm | | 42.5 | 42.0 | 42.4 | 42.1 | 0.7 | 3.6 |
| NGC 5253 | 3.2 | I0 | | 42.4 | 41.7 | 42.2 | 41.9 | 0.7 | 5.5 |
| NGC 253 | 3.0 | Sc | | 43.7 | 43.5 | 43.6 | 41.8 | 0.9 | 1.4 |
| NGC 628 | 9.7 | Sc | | 43.6 | 43.1 | 43.2 | 42.8 | 0.4 | 1.7 |
| NGC 1291 | 8.6 | SBa | | 43.7 | 43.6 | 42.1 | 42.1 | 0.02 | 0.06 |
| NGC 2681 | 13.3 | Sa | | 43.4 | 43.3 | 42.9 | 41.9 | 0.3 | 0.5 |
| NGC 3079 | 15.0 | Sc pec: | S2 | 43.7 | 43.5 | 43.8 | 42.2 | 1.3 | 2.4 |
| NGC 3184 | 8.7 | Sc | | 43.3 | 42.9 | 42.8 | 42.6 | 0.3 | 1.3 |
| NGC 3628 | 7.7 | Sbc | | 43.6 | 43.3 | 43.3 | 42.4 | 0.5 | 1.1 |
| NGC 4244 | 3.1 | Scd | | 42.8 | 41.8 | 41.6 | 41.6 | 0.06 | 1.3 |
| NGC 4258 | 6.8 | Sb | S1.9 | 43.8 | 43.5 | 43.0 | 42.4 | 0.2 | 0.4 |
| NGC 4314 | 9.7 | SBa | | 43.0 | 43.0 | 42.4 | 41.6 | 0.2 | 0.3 |
| NGC 4579 | 20.3 | Sab | S1.9/L1.9 | 44.0 | 44.0 | 43.3 | 42.7 | 0.2 | 0.2 |
| NGC 4631 | 6.9 | Sc | | 43.8 | 43.1 | 43.3 | 42.9 | 0.3 | 2.3 |
| NGC 4736 | 4.3 | RSab | | 43.3 | 43.2 | 42.9 | 42.3 | 0.4 | 0.6 |
| NGC 4945 | 5.2 | Sc | AGN | 44.0 | 43.7 | 43.8 | 41.7 | 0.6 | 1.4 |
| NGC 5194/5 | 7.7 | Sbc/SB | S2 | 43.9 | 43.8 | 43.3 | 43.1 | 0.2 | 0.5 |
| NGC 5236 | 4.7 | SBc | | 43.7 | 43.5 | 43.2 | 42.5 | 0.4 | 0.7 |
| NGC 5457 | 5.4 | Sc | | 43.7 | 43.1 | 43.3 | 43.4 | 0.4 | 3.2 |
| NGC 6503 | 6.1 | Sc | | 43.1 | 42.7 | 42.4 | 42.0 | 0.2 | 0.8 |
| NGC 1395 | 22.7 | E2 | | 44.0 | 43.9 | 41.6 | 42.3 | 0.003 | 0.03 |
| NGC 1399 | 19.3 | E1 | | 43.9 | 44.0 | 41.3 ^a | 42.5 | 0.002 | 0.03 |
| NGC 3379 | 8.1 | E0 | | 43.3 | 43.3 | <40.3 | 41.7 | <0.001 | <0.02 |
| NGC 4374 | 16.8 | E1 | | 44.0 | 44.0 | 42.0 | 42.4 | 0.01 | 0.04 |
| NGC 4472 | 16.8 | E1/S0 | S2:: | 44.3 | 44.3 | <41.1 | 42.8 | <0.0006 | <0.03 |
| NGC 4636 | 14.6 | E0/S0 | | 43.7 | 43.7 | 41.2 ^a | 42.4 | 0.003 | 0.05 |
| NGC 4649 | 14.9 | S0 | | 44.0 | 44.1 | 42.0 | 42.5 | 0.01 | 0.03 |
| NGC 4697 | 16.5 | E6 | | 43.9 | 43.9 | 42.0 | 42.3 | 0.01 | 0.04 |
| NGC 5128 | 4.9 | S0+S pec | AGN | 44.0 | 43.8 | 43.4 | 42.5 | 0.3 | 0.4 |

Notes on columns: (1) Galaxy name; (2) Distance to galaxy (see section 2); (3) Galaxy morphological type, from the RSA galaxy catalog (Sandage & Tammann 1981); (4) AGN type, as listed in Ho et al. (1997). We have additionally classified NGC 4945 and NGC 5128 as AGN, due to hard X-ray spectra properties, and nuclear jet, respectively. Blank entries denote LINER 1.9/2, transition, and H II classifications from Ho et al., or no evidence for AGN activity in the NED notes for that galaxy. (5) Galaxy B-band luminosity $\nu L\nu$, calculated using B_T^0 (or m_B^0 for NGC 4038/9) magnitudes from RC3; (6) Galaxy K_s-band luminosity $\nu L\nu$, calculated from 20 mag/sq. arcsec isophotal magnitudes from the 2MASS Large Galaxy Atlas (Jarrett et al. 2003); (7) Galaxy FIR luminosities, calculated from IRAS fluxes using the method of Fullmer & Lonsdale (1989). IRAS fluxes were taken preferentially from Moshir et al. (1997, as listed in NED), Soifer et al. (1989), Rice et al. (1988), Knapp (1994), Knapp et al. (1989), and Thronson et al. (1987); (8) Galaxy far-ultraviolet luminosity (see section 3.3); (9) Ratio of FIR to B-band luminosity; (10) Ratio of FIR+UV to K_s luminosity.

^aOnly upper limits were available for the 60 μ IRAS flux for NGC 1399 and the 100 μ flux for NGC 4636 (NED 1994 ref). The L_{FIR} value listed here was calculated using 50% of the quoted upper limit. The corresponding uncertainties in L_{FIR} due to this estimate are 0.05 and 0.08 dex for NGC 1399 and NGC 4636, respectively.

Table 3. Galaxy X-ray Properties

| Galaxy Name (1) | N_H (Gal) ($\log \text{cm}^{-2}$) (2) | L_X (limit) ($\log \text{erg/s}$) (3) | L_{XP} ($\log \text{erg/s}$) (4) | fraction $\geq 10^{38}$ L_{XP} (5) | fraction $\geq 10^{38}$ N (6) | fraction $\geq 10^{39}$ L_{XP} (7) | fraction $\geq 10^{39}$ N (8) | $\log(\frac{L_{XP}}{L_K})$ (9) |
|--------------------|---|---|--|--|-------------------------------------|--|-------------------------------------|-----------------------------------|
| NGC 1569 | 21.4 | 35.4 | 37.9 | 0.00 | 0.00(0) | 0.00 | 0.00(0) | -3.4 |
| NGC 3034 | 20.6 | 36.9 | 40.0 | 0.97 | 0.56(15) | 0.61 | 0.11(3) | -3.6 |
| NGC 4038/9 | 20.6 | 37.7 | 40.8 | 0.99 | 0.82(53) | 0.77 | 0.22(14) | -3.0 |
| NGC 4449 | 20.1 | 36.3 | 39.0 | 0.66 | 0.14(3) | 0.00 | 0.00(0) | -3.0 |
| NGC 5253 | 20.6 | 36.2 | 38.0 | 0.00 | 0.00(0) | 0.00 | 0.00(0) | -3.6 |
| NGC 253 | 20.2 | 36.7 | 39.4 | 0.65 | 0.12(6) | 0.00 | 0.00(0) | -4.1 |
| NGC 628 | 20.7 | 37.2 | 39.6 | 0.54 | 0.15(9) | 0.00 | 0.00(0) | -3.6 |
| NGC 1291 | 20.3 | 37.6 | 39.7 | 0.65 | 0.23(13) | 0.00 | 0.00(0) | -3.8 |
| NGC 2681 | 20.4 | 37.2 | 39.7 | 0.93 | 0.53(9) | 0.59 | 0.12(2) | -3.6 |
| NGC 3079 | 19.9 | 37.7 | 39.6 | 0.84 | 0.41(7) | 0.43 | 0.06(1) | -3.8 |
| NGC 3184 | 20.0 | 37.1 | 39.4 | 0.44 | 0.07(3) | 0.00 | 0.00(0) | -3.5 |
| NGC 3628 | 20.3 | 36.8 | 39.5 | 0.71 | 0.09(3) | 0.63 | 0.03(1) | -3.9 |
| NGC 4244 | 20.2 | 36.1 | 37.6 | 0.00 | 0.00(0) | 0.00 | 0.00(0) | -4.2 |
| NGC 4258 | 20.1 | 37.3 | 39.6 | 0.83 | 0.42(11) | 0.00 | 0.00(0) | -3.8 |
| NGC 4314 | 20.3 | 37.9 | 39.0 | 0.66 | 0.33(4) | 0.00 | 0.00(0) | -3.9 |
| NGC 4579 | 20.4 | 37.9 | 40.2 | 1.00 | 1.00(8) | 0.87 | 0.25(2) | -3.8 |
| NGC 4631 | 20.1 | 36.7 | 39.5 | 0.86 | 0.20(5) | 0.53 | 0.04(1) | -3.6 |
| NGC 4736 | 20.2 | 36.4 | 39.6 | 0.90 | 0.29(8) | 0.55 | 0.07(2) | -3.6 |
| NGC 4945 | 21.2 | 37.6 | 39.8 | 0.88 | 0.39(14) | 0.39 | 0.06(2) | -3.8 |
| NGC 5194/5 | 20.2 | 37.4 | 40.0 | 0.84 | 0.33(17) | 0.33 | 0.04(2) | -3.8 |
| NGC 5236 | 20.6 | 36.5 | 39.8 | 0.69 | 0.17(14) | 0.18 | 0.01(1) | -3.7 |
| NGC 5457 | 20.1 | 36.3 | 39.8 | 0.66 | 0.06(8) | 0.25 | 0.01(1) | -3.4 |
| NGC 6503 | 20.6 | 37.4 | 39.1 | 0.85 | 0.43(3) | 0.00 | 0.00(0) | -3.6 |
| NGC 1395 | 20.3 | 38.4 | 40.2 | 1.00 | 1.00(30) | 0.49 | 0.10(3) | -3.7 |
| NGC 1399 | 20.1 | 37.6 | 40.4 | 0.91 | 0.74(74) | 0.23 | 0.03(3) | -3.6 |
| NGC 3379 | 20.4 | 37.1 | 39.5 | 0.73 | 0.23(8) | 0.00 | 0.00(0) | -3.8 |
| NGC 4374 | 20.4 | 37.8 | 40.2 | 0.98 | 0.86(24) | 0.63 | 0.04(1) | -3.8 |
| NGC 4472 | 20.2 | 37.7 | 40.3 | 0.96 | 0.87(68) | 0.14 | 0.03(2) | -4.0 |
| NGC 4636 | 20.3 | 37.5 | 39.6 | 0.69 | 0.49(18) | 0.00 | 0.00(0) | -4.1 |
| NGC 4649 | 20.3 | 37.8 | 40.2 | 0.80 | 0.56(55) | 0.07 | 0.01(1) | -3.9 |
| NGC 4697 | 20.3 | 37.6 | 40.1 | 0.86 | 0.58(40) | 0.11 | 0.01(1) | -3.8 |
| NGC 5128 | 20.9 | 36.9 | 40.1 | 0.66 | 0.19(25) | 0.15 | 0.01(1) | -3.8 |

Notes on columns: (1) Galaxy Name; (2) Neutral Hydrogen absorption column of the Milky Way, from the FTOOLS NH program (Dickey & Lockman 1990); (3) Limiting X-ray luminosity calculated using PIMMS, assuming a detection of 10 net counts, a power-law model with photon index $\Gamma = 1.7$, and the Galactic absorption listed in column 2. Since most of the galaxies were centered on CCD7 and most of the point sources were positioned on that chip, we assumed the spectral response for CCD7, and the exposure time for CCD7 listed in Table 1, except for the following galaxies: NGC 3034 (CCD0), NGC 1395 (CCD3), and NGC 5128 (CCD0). (4) Observed X-ray point-source luminosity, from all point sources (see Table 1, column 6). Note that nuclear and near-nuclear (within 5" of the NED astrometric position) X-ray point sources have been omitted for the following galaxies: NGC 3079, NGC 4258, NGC 4579, NGC 4945, NGC 5194, NGC 4374, and NGC 5128. Artificial X-ray sources due to saturation along the CCD readout direction ("readout stripes") have been omitted for NGC 4579 and NGC 5128. X-ray sources along the "jet" in NGC 5128 have also been omitted. (5,6) Fraction of L_{XP} and N (the number of X-ray point sources listed in Table 1) from sources with $L_X \geq 10^{38} \text{ erg s}^{-1}$. The number of sources with $L_X \geq 10^{38} \text{ erg s}^{-1}$ is listed in parentheses in column 6; (7,8) Same as columns (5,6) except for $10^{39} \text{ erg s}^{-1}$; (9) Ratio of L_{XP} to galaxy K_s band luminosity from Table 2.

Table 4. Slopes of Cumulative X-ray Luminosity Functions

| Galaxy Name (1) | $\bar{L}_X(\min)$ (log erg/s) (2) | $\bar{L}_X(\max)$ (log erg/s) (3) | N (4) | γ (5) |
|--------------------|---|---|----------|-----------------|
| NGC 1569 | 36.0 | 37.5 | 5 | 0.44 |
| NGC 3034 | 37.5 | 39.5 | 20 | 0.57 |
| NGC 4038/9 | 38.0 | 40.0 | 53 | 0.63 |
| NGC 4449 | 37.0 | 38.4 | 12 | 0.70 |
| NGC 5253 | 36.5 | 37.7 | 8 | 0.92 |
| NGC 253 | 37.0 | 38.6 | 36 | 0.75 |
| NGC 628 | 37.5 | 38.6 | 38 | 1.11 |
| NGC 1291 | 37.7 | 38.9 | 31 | 1.16 |
| NGC 2681 | 37.8 | 39.2 | 10 | 0.65 |
| NGC 3079 | 37.5 | 39.2 | 17 | 0.80 |
| NGC 3184 | 37.5 | 38.7 | 20 | 1.15 |
| NGC 3628 | 37.0 | 39.3 | 28 | 0.82 |
| NGC 4244 | 36.6 | 37.5 | 3 | 0.46 |
| NGC 4258 | 37.5 | 38.8 | 23 | 0.79 |
| NGC 4314 | 37.7 | 38.2 | 7 | 1.20 |
| NGC 4579 | 38.5 | 40.1 | 5 | 0.47 |
| NGC 4631 | 37.0 | 39.2 | 23 | 0.69 |
| NGC 4736 | 37.2 | 39.1 | 19 | 0.55 |
| NGC 4945 | 37.6 | 39.1 | 22 | 0.70 |
| NGC 5194/5 | 37.7 | 39.1 | 29 | 0.78 |
| NGC 5236 | 37.5 | 39.0 | 34 | 0.91 |
| NGC 5457 | 37.0 | 39.2 | 68 | 0.85 |
| NGC 6503 | 37.5 | 38.7 | 4 | 0.37 |
| NGC 1395 | 38.3 | 39.7 | 22 | 1.05 |
| NGC 1399 | 38.0 | 39.4 | 79 | 1.26 |
| NGC 3379 | 37.8 | 39.0 | 12 | 1.07 |
| NGC 4374 | 38.0 | 38.6 | 26 | 1.16 |
| NGC 4472 | 38.5 | 39.2 | 19 | 1.63 |
| NGC 4636 | 38.0 | 38.6 | 22 | 2.36 |
| NGC 4649 | 38.0 | 39.0 | 62 | 1.58 |
| NGC 4697 | 38.0 | 39.1 | 39 | 1.34 |
| NGC 5128 | 38.0 | 39.2 | 28 | 1.28 |

Notes on columns: (1) Galaxy Name; (2,3) The slope γ was computed using a weighted least-squares algorithm with logarithmic bins in X-ray luminosity. $\bar{L}_X(\min)$ and $\bar{L}_X(\max)$ are the luminosities corresponding to (the center of) the minimum and maximum bin used to compute γ . The bins have width of 0.1 dex. $\bar{L}_X(\min)$ was chosen to maximize the range in $L_{X,P}$ without including very low $L_{X,P}$ values, where a completeness problem may exist (see Figures 2 and 3). (4) Total number of X-ray point sources used in the fit; (5) Slope γ of the cumulative XLF

Table 5. Inferred Properties of Host Galaxies

| Galaxy Name (1) | SFR ($M_{\odot} \text{ yr}^{-1}$) (2) | $\log(M/L)_K$ (\odot) (3) | Mass $\log(M_{\odot})$ (4) |
|--------------------|---|-------------------------------------|----------------------------------|
| NGC 1569 | 0.037 | −0.6 | 7.9 |
| NGC 3034 | 9.3 | −0.1 | 10.8 |
| NGC 4038/9 | 8.3 | −0.4 | 10.7 |
| NGC 4449 | 0.21 | −0.4 | 8.9 |
| NGC 5253 | 0.14 | −0.5 | 8.4 |
| NGC 253 | 2.4 | −0.3 | 10.5 |
| NGC 628 | 1.3 | −0.4 | 10.0 |
| NGC 1291 | 0.13 | −0.2 | 10.7 |
| NGC 2681 | 0.47 | −0.3 | 10.3 |
| NGC 3079 | 4.0 | −0.3 | 10.5 |
| NGC 3184 | 0.56 | −0.4 | 9.8 |
| NGC 3628 | 1.3 | −0.3 | 10.3 |
| NGC 4244 | 0.047 | −0.7 | 8.4 |
| NGC 4258 | 0.69 | −0.3 | 10.4 |
| NGC 4314 | 0.16 | −0.2 | 10.1 |
| NGC 4579 | 1.4 | −0.2 | 11.1 |
| NGC 4631 | 1.6 | −0.5 | 9.8 |
| NGC 4736 | 0.58 | −0.2 | 10.4 |
| NGC 4945 | 3.6 | −0.3 | 10.6 |
| NGC 5194/5 | 1.8 | −0.2 | 10.8 |
| NGC 5236 | 1.2 | −0.3 | 10.5 |
| NGC 5457 | 2.5 | −0.5 | 10.0 |
| NGC 6503 | 0.20 | −0.4 | 9.6 |
| NGC 1395 | ... | −0.2 | 11.0 |
| NGC 1399 | ... | −0.1 | 11.2 |
| NGC 3379 | ... | −0.1 | 10.5 |
| NGC 4374 | ... | −0.2 | 11.1 |
| NGC 4472 | ... | −0.1 | 11.5 |
| NGC 4636 | ... | −0.1 | 10.9 |
| NGC 4649 | ... | −0.1 | 11.2 |
| NGC 4697 | ... | −0.2 | 11.0 |
| NGC 5128 | 1.7 ^a | −0.2 | 10.9 |

Notes on columns: (1) Galaxy name; (2) Star formation rate, estimated from L_{FIR+UV} (see text section 5.2); (3) Stellar mass-to-light ratio for the K band, in solar units, calculated from B−K (Table 2). See text section 5.2 for details; (4) Stellar mass, calculated using L_K from Table 2, and $(M/L)_K$ from column 3.

^aSince the FIR emission from elliptical galaxies is not necessarily dominated by re-radiated emission from hot stars, it may not be a good predictor of the SFR in elliptical galaxies. However, since NGC 5128 does have ongoing star formation, we have estimated a SFR for it.

Table 6. Proportionality Constants for L_{XP}

| A (1) | B (2) | χ^2_ν (3) | α (4) | β (5) | χ^2_ν (6) | Sample Description (No. of galaxies) (7) |
|------------------------|------------------------|---------------------|------------------------|------------------------|---------------------|---|
| $1.26^{+0.30}_{-0.31}$ | ... | 0.81 | $0.88^{+0.22}_{-0.21}$ | ... | 0.90 | Elliptical galaxies only (8) |
| $1.11^{+0.11}_{-0.11}$ | $0.31^{+0.10}_{-0.10}$ | 4.61 | $1.05^{+0.11}_{-0.11}$ | $0.74^{+0.15}_{-0.15}$ | 3.79 | All galaxies with FIR flux measurements (30) |
| $1.01^{+0.14}_{-0.14}$ | $0.44^{+0.14}_{-0.13}$ | 5.53 | $1.09^{+0.14}_{-0.14}$ | $0.86^{+0.19}_{-0.19}$ | 4.40 | All galaxies with FIR flux measurements, excepting AGN (24) |
| $0.93^{+0.15}_{-0.15}$ | $0.49^{+0.14}_{-0.13}$ | 7.21 | $1.25^{+0.17}_{-0.17}$ | $0.74^{+0.20}_{-0.18}$ | 5.56 | Only M/I and Spiral galaxies, no AGN (18) |

Notes on columns: (1,2) Dimensionless A and B constants for correlation of L_{XP} with host galaxy luminosities L_K and L_{FIR+UV} , respectively (see section 5.3, equation 1); (3) Reduced- χ^2 for the fit = χ^2 / (no. of galaxies - no. of parameters); (4,5) Constants α and β , for correlation with M and SFR (see equation 2). Units are $\text{erg s}^{-1} \text{M}_\odot$ and $\text{erg s}^{-1} (\text{M}_\odot \text{yr}^{-1})^{-1}$, respectively; (6) Reduced- χ^2 for the fit; (7) Description of the galaxy sample used in the calculation (number of galaxies in parentheses)

All quoted uncertainties are 90% confidence for one parameter free ($\Delta\chi^2 = 2.7$). For example, errors in A were determined by fixing B at its minimum- χ^2 value and scanning over A .